# Spectroscopic and Electronic Structure Description of the Reduced Binuclear Non-Heme Iron Active Site in Ribonucleotide Reductase from *E. coli*: Comparison to Reduced $\Delta^9$ Desaturase and Electronic Structure Contributions to Differences in $O_2$ Reactivity

**Yi-Shan Yang,[†] Jeffrey Baldwin,[‡] Brenda A. Ley,[‡] J. Martin Bollinger, Jr.,*[,‡] and Edward I. Solomon*[,†]**

*Contribution from the Department of Chemistry, Stanford University, Stanford, California 94305, and the Department of Biochemistry and Molecular Biology, The Pennsylvania State University, University Park, Pennsylvania 16802*

*Received December 16, 1999. Revised Manuscript Received May 12, 2000*

**Abstract:** Ribonucleotide reductase (RR) catalyzes the first committed and rate-determining step in DNA biosynthesis, the reduction of ribonucleotides to deoxyribonucleotides. $Fe^{II}$ binding to the binuclear non-heme iron active site has been studied using a combination of circular dichroism (CD), magnetic circular dichroism (MCD), and variable-temperature variable-field (VTVH) MCD spectroscopies. These studies show that the two sites have significantly different metal binding affinities. This has also allowed a $Mn^{II}Fe^{II}$ derivative to be prepared and studied by the above spectroscopies. The spectral features of the individual irons provide geometric and electronic structural insight into each metal site. Density functional calculations on reduced RR are correlated to the spectral features to obtain insight into its electronic structure. Parallel calculations are also performed on reduced stearoyl-acyl carrier protein $\Delta^9$ desaturase ($\Delta^9$D) to correlate to prior spectral data and to the active site of RR. Differences in their dioxygen reactivities are investigated through reaction of these reduced sites with dioxygen, and possible electron-transfer pathways are evaluated. These results show that the active site of reduced RR consists of one 5- and one 4-coordinate iron with the 5C center having a higher binding affinity. Compared to reduced $\Delta^9$D, the presence of the 4C site energetically destabilizes reduced RR. Reaction of reduced RR with dioxygen to form a superoxide intermediate is energetically up hill as it results in an excited quartet state on the oxygenated iron, while the formation of a bridged peroxo intermediate is energetically favorable. Formation of peroxo-RR is more favorable than peroxo-$\Delta^9$D due to ligand field differences that can control the overlap of the redox active orbitals of the reduced sites with the $\pi^*$ orbitals of dioxygen. This parallels experimental differences in the dioxygen reactivity of the reduced RR and $\Delta^9$D active sites.

## Introduction

A number of binuclear non-heme iron active sites have been found in a variety of metalloproteins and enzymes that are involved in reactions with dioxygen.[1−9] The binuclear centers all show magnetic coupling associated with bridging ligands and can exist in different oxidation states, including the met or oxidized [$Fe^{III}Fe^{III}$], half-met or mixed valent [$Fe^{II}Fe^{III}$], and deoxy or reduced [$Fe^{II}Fe^{II}$] forms.[10−19] Among these binuclear non-heme iron proteins, methane monooxygenase (MMO), ribonucleotide reductase (RR), and stearoyl-acyl carrier protein $\Delta^9$ desaturase ($\Delta^9$D) have been found to share similarities in their amino acid primary sequences and the physical properties of their binuclear active sites.[20−22] They all activate dioxygen

[†] Stanford University.
[‡] The Pennsylvania State University.

(1) Stenkamp, R. E. *Chem. Rev.* **1994**, *94*, 715−726.
(2) Wallar, B. J.; Lipscomb, J. D. *Chem. Rev.* **1996**, *96*, 2625−2657.
(3) Pikus, J. D.; Studts, J. M.; Achim, C.; Kauffmann, K. E.; Münck, E.; Steffan, R. J.; McClay, K.; Fox, B. G. *Biochemistry* **1996**, *35*, 9106−9119.
(4) Shanklin, J.; Cahoon, E. B. *Annu. Rev. Plant Physiol. Plant Mol. Biol.* **1998**, *49*, 611−641.
(5) Klabunde, T.; Krebs, B. *Struct. Bonding* **1997**, *89*, 177−198.
(6) Coulter, E. D.; Shenvi, N. V.; Kurtz, D. M., Jr. *Biochem. Biophys. Res. Commun.* **1999**, *255*, 317−323.
(7) Gdaniec, Z.; Sierzputowska, G. H.; Theil, E. C. *Biochemistry* **1999**, *38*, 5676.
(8) Shanklin, J.; Achim, C.; Schmidt, H.; Fox, B. G.; Münck, E. *Proc. Natl. Acad. Sci. U.S.A.* **1997**, *94*, 2981−2986.
(9) Feig, A. L.; Lippard, S. J. *Chem. Rev.* **1994**, *94*, 759−80.
(10) Holmes, M. A.; Trong, I. L.; Turley, S.; Sieker, L. C.; Stenkamp, R. E. *J. Mol. Biol.* **1991**, *218*, 633−593.
(11) Holmes, M. A.; Stenkamp, R. E. *J. Mol. Biol.* **1991**, *220*, 723−737.
(12) Rosenzweig, A. C.; Frederick, C. A.; Lippard, S. J.; Nordlund, P. *Nature* **1993**, *366*, 537−543.
(13) Rosenzweig, A. C.; Nordlund, P.; Takahara, P. M.; Frederick, C. A.; Lippard, S. J. *Chem. Biol.* **1995**, *2*, 409−418.
(14) Nordlund, P.; Sjöberg, B.-M.; Eklund, H. *Nature* **1990**, *45*, 593−598.
(15) Logan, D. T.; Su, X.-D.; Åberg, A.; Regnström, K.; Hajdu, J.; Eklund, H.; Nordlund, P. *Structure* **1996**, *4*, 1053−1064.
(16) Lindqvist, Y.; Huang, W.; Schneider, G.; Shanklin, J. *The EMBO J.* **1996**, *15*, 4081−4092.
(17) Klabunde, T.; Sträter, N.; Fröhlich, R.; Witzel, H.; Krebs, B. *J. Mol. Biol.* **1996**, *259*, 737−748.
(18) deMaré, F.; Donald, M.; Kurtz, J.; Nordlund, P. *Nature Struct. Biol.* **1996**, *3*, 539−546.
(19) Ha, Y.; Shi, D. S.; Small, G. W.; Theil, E. C.; Allewell, N. M. *J. Bioinorg. Chem.* **1999**, *4*, 243−256.
(20) Bollinger, J. M., Jr.; Edmondson, D. E.; Huynh, B. H.; Filley, J.; Norton, J. R.; Stubbe, J. *Science* **1991**, *253*, 292−298.
(21) Bollinger, J. M., Jr.; Krebs, C.; Vicol, A.; Chen, S.; Ley, B. A.; Edmondson, D. E.; Huynh, B. H. *J. Am. Chem. Soc.* **1998**, *120*, 1094−109.

10.1021/ja994406r CCC: $19.00 
Published on Web 08/18/2000

and similar intermediates, including $(Fe^{III})_2$-peroxo and high-valent $Fe^{IV}$-oxo species have been observed.[21,23−33] These enzymes, however, perform different catalytic functions that involve significantly different dioxygen reactivity. MMO catalyzes the most energetic step in the degradation of methane to convert it to methanol.[2,34,35] The hydroxylase component contains a reduced binuclear non-heme active site that slowly reacts with dioxygen. This reactivity is greatly enhanced (by ∼1000-fold) by the addition of a small coupling protein, component B.[36,37] Reduced $\Delta^9$D inserts a cis-double bond in fatty acid biosynthesis to convert stearoyl-ACP to oleoyl-ACP.[38] The resting reduced site also does not efficiently react with dioxygen until substrate (stearoyl-ACP) is present.[26,38,39] RR catalyzes the reduction of ribonucleotides to deoxyribonucleotides that is the first committed and rate-determining step in DNA biosynthesis.[40−42] Class I RR from *E. coli* is a two-component enzyme consisting of homodimeric R1 and R2 subunits. The R2 subunit contains one binuclear non-heme iron active site that in the binuclear ferrous state reacts with dioxygen to generate a tyrosyl radical that is essential for the catalytic reaction that occurs at the R1 subunit.[14,43−46] In contrast to the above enzymes, reduced R2 does react rapidly with dioxygen as the substrate, a tyrosine residue, is already present at the site.[39,47] It is thus of importance to understand how these sites relate to each other and how the reactive reduced sites relate to the crystal structures.

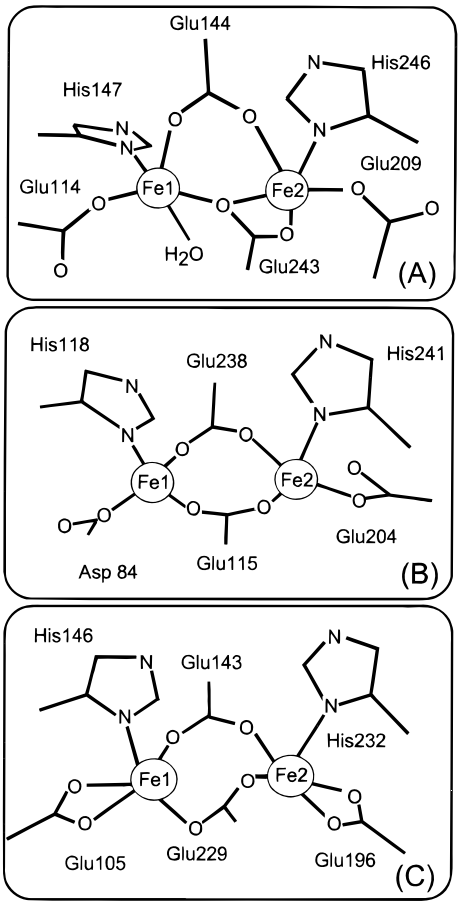


**Figure 1.** Representations of the crystallographically determined binuclear $Fe^{II}Fe^{II}$ active sites of (A) methane monooxygenase, (B) ribonucleotide reductase from *E. coli* (1XIK), and (C) stearoyl-acyl carrier protein $\Delta^9$ desaturase (1AFR). The structure in A was adapted from ref 13. The structures B and C were generated using the crystallographic coordinates from the indicated PDB files. The structure in A was reprinted with permission from Elsevier Science (1995, Ref 13).

Crystal structures of the reduced active sites of MMO, RR, and $\Delta^9$D have been reported (Figure 1) and provide the starting point for an in-depth understanding of their dioxygen reactivity.[13,15,16] The reduced structure of MMOH (Figure 1A) contains two iron centers bridged by one $\mu$-1,3 and one $\mu$-1,1 carboxylate ligand. One histidine and one monodentate glutamate are coordinated to each iron. An additional terminal water is bound to Fe1. Both iron centers are 5-coordinate. The Fe−Fe distance is 3.3 Å. Reduced RR (Figure 1B) contains two irons separated by 3.9 Å. His241 and monodentate Glu204 are bound to Fe2. Fe1 coordinates His118 and monodentate Asp84. Glu238 and Glu115 bridge the two irons in a $\mu$-1,3 configuration. Both iron centers are 4-coordinate. The binuclear ferrous active site of $\Delta^9$D (Figure 1C) has two iron centers that are approximately equivalent with one histidine and one bidentate glutamate. The two irons are bridged by two $\mu$-1,3 carboxylate ligands, resulting in an Fe−Fe distance of about 4.2 Å. The active site coordination geometry of the RR crystal structure is not completely consistent with the one obtained from circular dichroism and magnetic circular dichroism studies (vide infra),[48] and the correlation between these two structures will be considered.

A combination of circular dichroism (CD), magnetic circular dichroism (MCD), and variable-temperature variable-field

(22) Kurtz, D. M. *J. Biol. Inorg. Chem.* **1997**, *2*, 159−167.
(23) Valentine, A. M.; Stahl, S. S.; Lippard, S. J. *J. Am. Chem. Soc.* **1999**, *121*, 3876−3887.
(24) Lee, S.-K.; Lipscomb, J. D. *Biochemistry* **1999**, *38*, 4423−4432.
(25) Moënne-Loccoz, P.; Baldwin, J.; Ley, B. A.; Loehr, T. M.; Bollinger, J. M., Jr. *Biochemistry* **1998**, *37*, 14659−14663.
(26) Broadwater, J. A.; Ai, J.; Loehr, T. M.; Sanders-Loehr, J.; Fox, B. G. *Biochemistry* **1998**, *37*, 14664−14671.
(27) Lee, S.-K.; Nesheim, J. C.; Lipscomb, J. D. *J. Biol. Chem.* **1993**, *268*, 21569−21577.
(28) Liu, K. E.; Valentine, A. M.; Qiu, D.; Edmondson, D. E.; Appelman, E. H.; Spiro, T. G.; Lippard, S. J. *J. Am. Chem. Soc.* **1997**, *119*, 11134−11134.
(29) Liu, K. E.; Valentine, A. M.; Wang, D. L.; Huynh, B. H.; Edmondson, D. E.; Salifoglou, A.; Lippard, S. J. *J. Am. Chem. Soc.* **1995**, *117*, 10174−10185.
(30) Ravi, N.; Bollinger, J. M., Jr.; Huynh, B. H.; Edmondson, D. E.; Stubbe, J. *J. Am. Chem. Soc.* **1994**, *116*, 8007−8014.
(31) Bollinger, J. M., Jr.; Tong, W. H.; Ravi, N.; Huynh, B. H.; Edmondson, D. E.; Stubbe, J. *J. Am. Chem. Soc.* **1994**, *116*, 8015−8023.
(32) Bollinger, J. M., Jr.; Tong, W. H.; Ravi, N.; Huynh, B. H.; Edmondson, D. E.; Stubbe, J. *J. Am. Chem. Soc.* **1994**, *116*, 8024−8032.
(33) Bollinger, J. M., Jr.; Ravi, N.; Tong, W. H.; Edmondson, D. E.; Huynh, B. H.; Stubbe, J. *J. Inorg. Biochem.* **1993**, *51*, 6.
(34) Dalton, H. *Adv. Appl. Microbiol.* **1980**, *26*, 71−87.
(35) Valentine, A. M.; Lippard, S. J. *J. Chem. Soc., Dalton Trans.* **1997**, 3925−3931.
(36) Liu, Y.; Nesheim, J. C.; Paulsen, K. E.; Stankovich, M. T.; Lipscomb, J. D. *Biochemistry* **1997**, *36*, 5223−5233.
(37) Liu, Y.; Nesheim, J. C.; Lee, S.-K.; Lipscomb, J. D. *J. Biol. Chem.* **1995**, *270*, 24662-24665.
(38) Fox, B. G.; Shanklin, J.; Ai, J. Y.; Loehr, T. M.; Sanders-Loehr, J. *Biochemistry* **1994**, *33*, 12776−12836.
(39) Yang, Y.-S.; Broadwater, J. A.; Pulver, S. C.; Fox, B. G.; Solomon, E. I. *J. Am. Chem. Soc.* **1999**, *121*, 2770−2783.
(40) Stubbe, J. *J. Biol. Chem.* **1990**, *265*, 5329−5332.
(41) Sjöberg, B.-M.; Gräslund, A. *Ribonucleotide Reductase*; Theil, E. C., Eichorn, G. L., Marzilli, L. G., Eds.; Elsevier: 1983; Vol. 5, pp 87−110.
(42) Reichard, P.; Ehrenberg, A. *Science* **1983**, *221*, 514−519.
(43) Nordlund, P.; Eklund, H. *J. Mol. Biol.* **1993**, *232*, 123−164.
(44) von Döbeln, U.; Reichard, P. *J. Biol. Chem.* **1976**, *251*, 3616−3622.
(45) Thelander, L. *J. Biol. Chem.* **1974**, *249*, 4858−4862.
(46) Uhlin, U.; Eklund, H. *Nature* **1994**, *370*, 533−539.
(47) Solomon, E. I.; Brunold, T.; Davis, M. I.; Kemsley, J. N.; Lee, S.-K.; Lehnert, N.; Neese, F.; Skulan, A. J.; Yang, Y.-S.; Zhou, J. *Chem. Rev.* **2000**, *100*, 235−349.
(48) Pulver, S. C.; Tong, W. H.; Bollinger, M. J., Jr.; Stubbe, J.; Solomon, E. I. *J. Am. Chem. Soc.* **1995**, *117*, 12664−12678.

(VTVH) MCD spectroscopies in the NIR region (5000−16000 $cm^{-1}$) provides direct probes of non-heme ferrous active sites.[49,50] These sites have been difficult to study since they are not easily accessible through the traditional techniques such as EPR and absorption spectroscopies. However, CD and MCD spectroscopies allow the observation of transitions to ligand field excited states that are weak in absorption. The high-spin $d^6$ ferrous ion in an octahedral ($O_h$) ligand field has an orbitally triply degenerate $^5T_{2g}$ ground state and a doubly degenerate $^5E_g$ excited state split by $10Dq_{Oh}$ that is about 10000 $cm^{-1}$ for biologically relevant nitrogen and oxygen ligands. The $^5T_{2g}$ and $^5E_g$ states further split in energy due to the low symmetry of the reduced active site.[49,50] Distorted 6-coordinate sites energetically split the $^5E$ state to produce a pair of transitions at around 10000 $cm^{-1}$ separated by up to ∼2000 $cm^{-1}$. Removal of an axial ligand leads to a five-coordinate square-pyramidal (SP) geometry that can show two transitions at around 5000 and >10000 $cm^{-1}$. Rearrangement of the five ligands toward a trigonal bipyramidal (TBP) geometry decreases the transition energies, resulting in ligand field transitions at <5000 and <10000 $cm^{-1}$. A four-coordinate ferrous site has $10Dq_{Td}$ equal to $-(4/9)10Dq_{Oh}$. Thus the highest energy ligand field transitions are in the 5000−7000 $cm^{-1}$ region. The VTVH MCD behavior of a ligand field transition can be further utilized to estimate the ground-state parameters of a coupled binuclear active site, including the total spin states and *g* values of the dimer ground and excited sublevels and the energies of the excited sublevels. These results can be further interpreted through a spin-Hamiltonian analysis to obtain the axial and rhombic zero-field splitting (ZFS) parameters *D* and *E* of each iron that give the splitting of the single site $^5T_{2g}$ state (vide supra) and the exchange coupling interaction (*J*) between the irons that reflects the bridging ligands.

By using a combination of CD/MCD/VTVH MCD in the NIR region, the binuclear active site of reduced RR has been found to exhibit spectral features corresponding to one 5C and one 4C iron site that are weakly antiferromagnetically coupled.[48] This result, however, does not directly correlate with the crystal structure in which both iron centers are 4-coordinate (with two $\mu$-1,3 carboxylate bridges associated with the weak antiferromagnetic coupling) (Figure 1B).[15] Recent Mössauer studies on reduced RR have indicated that the two metal centers of apo RR have differential binding affinities for ferrous ion.[51] In this study a series of CD/MCD/VTVH MCD titrations are performed on apo RR with ferrous ion to determine the spectral features of each metal binding site and estimate its binding constant. The single site geometric and electronic structures are obtained from these titrations and a MnFe derivative is prepared based on the differential metal binding affinities. The active site structure obtained is correlated to the crystal structure results. Furthermore, a series of density functional calculations are performed on reduced RR and reduced $\Delta^9$D to correlate to the spectral features and gain insight into active site electronic structures. These protein sites have large differences in dioxygen reactivity. Thus the experimentally calibrated active site structures are further utilized to explore the possible origin of these differences through the reaction of these sites with dioxygen. Two intermediates are considered to investigate their possible participation in the reaction coordinate: (1) dioxygen binding to one iron in an end-on fashion that is found to generate a superoxide species and (2) dioxygen binding to both irons in a $\mu$-1,2 bridging configuration that allows two-electron transfer and the formation of a peroxide intermediate. These results demonstrate that reduced RR contains one 5C and one 4C iron site that serves as a common structure for the dioxygen reactive forms of RR and $\Delta^9$D (in the presence of substrate). Relative to reduced $\Delta^9$D, the presence of the 4C site destabilizes reduced RR and rotates the redox active orbital such that there is now good overlap for two-electron transfer to the $\pi^*$ orbitals of dioxygen to form a bridged peroxo intermediate.

(49) Pulver, S.; Froland, W. A.; Fox, B. G.; Lipscomb, J. D.; Solomon, E. I. *J. Am. Chem. Soc.* **1993**, *115*, 12409−12422.

(50) Reem, R. C.; Solomon, E. I. *J. Am. Chem. Soc.* **1987**, *109*, 1216−1226.

(51) Bollinger, J. M., Jr.; Chen, S.; Parkin, S. E.; Mangravite, L. M.; Ley, B. A.; Edmondson, D. E.; Huynh, B. H. *J. Am. Chem. Soc.* **1997**, *119*, 5976−5977.

## Experimental Section

All commercial reagents were used as obtained: HEPES buffer (Sigma, Mallinckrodt), sodium chloride (Sigma), ferrous ammonium sulfate hexahydrate (Mallinckrodt), manganese chloride quadrahydrate (Mallinckrodt), deuterium oxide (99.9 atom % D, Aldrich), and $d_3$-glycerol (98 atom %, Cambridge Isotope Laboratories). Prior to use in an inert atmosphere, deuterated buffer was degassed by purging with 99.9% pure Argon gas for at least 1 h; $d_3$-glycerol was degassed with at least 5 freeze−pump−thaw cycles at $10^{-3}$ Torr. Protein samples were degassed by rapidly purging with at least 20 vacuum/argon cycles; solid ferrous ammonium sulfate, manganese chloride, and sodium chloride were pumped at $10^{-3}$ KPa for at least 30 min.

The R2 subunit of ribonucleotide reductase was expressed, purified, and characterized as previously described.[25] Purified protein obtained as the apo form was concentrated to ∼2 mM by ultrafiltration (Amicon stirred ultrafiltration cell, Beverly, MA) using YM30 membranes. Deuterated buffer (0.15 M Hepes, pD 7.6) was added and the solution was concentrated to ∼2 mM protein. This process was repeated until the percentage of $D_2O$ was greater than 99.9% of the solvent and the protein concentration was ∼2 mM. The concentration of reduced R2 was determined by conversion to native R2 ($\epsilon_{280} = 131$ $mM^{-1}$ $cm^{-1}$).

Ferrous and manganese solutions were obtained by anaerobically dissolving ferrous ammonium sulfate and manganese chloride in degassed deuterated buffer to a final concentration of 50 mM. Sodium chloride solutions were obtained by anaerobically dissolving solid sodium chloride in degassed deuterated buffer to a final concentration of 2 M. The appropriate amount of the ferrous or manganous solution was added anaerobically to the apo protein and the solution was incubated for at least 5 min. The sample was then transferred to an anaerobic cuvette for CD measurements. The MCD sample was prepared by anaerobic addition of 50−60% (v/v) $d_3$-glycerol to the $Fe^{II}$-loaded R2 protein that was then transferred into a pre-assembled MCD cell. The sample was then immediately frozen in liquid nitrogen.

Circular dichroism studies were performed on a JASCO J-200D spectropolarimeter operating with a liquid nitrogen-cooled InSb detector in the 600−2000-nm region. Low-temperature magnetic circular dichroism data were acquired on this spectropolarimeter, modified to accommodate an Oxford Instruments SM4000-7T superconducting magnet capable of magnetic fields up to 7.0 T and temperatures down to 1.6 K.

Protein samples prepared for MCD studies were slowly inserted into the cryostat to reduce strain in the resulting optical glass. The depolarization of the protein glass was checked by measuring the CD spectrum of a freshly prepared nickel (+)-tartrate solution placed immediately before and after the MCD sample. Typically, less than ∼5% of depolarization was observed.

The baseline-corrected CD and MCD spectra were fit to Gaussian band shapes using a constrained nonlinear least-squares fitting procedure. Each spectroscopic method has different selection rules; thus, transitions can have different intensities and signs but the energies are similar. The MCD spectra are taken at low temperature; thus, they may have significantly narrower bandwidths and the band energies may shift by a limited amount relative to those in the room-temperature CD spectra, which were allowed to float in the final fit. VTVH MCD data (MCD intensity, temperature, and applied magnetic field) were fit using a simplex routine that minimizes the $\chi$-squared value. A goodness of fit parameter ($\chi$-square/number of float parameters) was utilized in the comparison of different fit results.

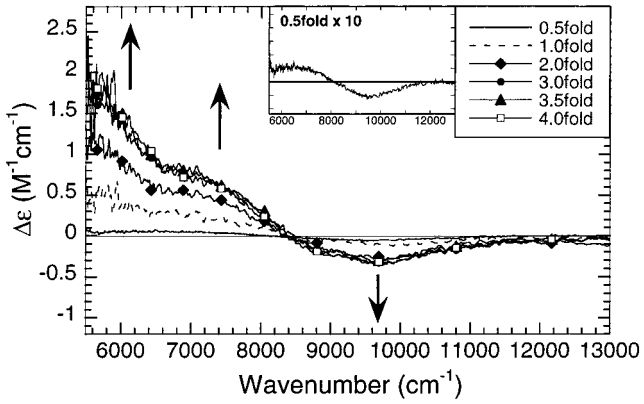


**Figure 2.** CD spectra at 5 °C of apo RR in the presence of a 0.5 (—), 1.0 (- - -), 2.0 (♦), 3.0 (●), 3.5 (▲), and 4.0 (□) molar equiv of ferrous ion. The 0.5-fold curve is expanded 10 times in the inset.

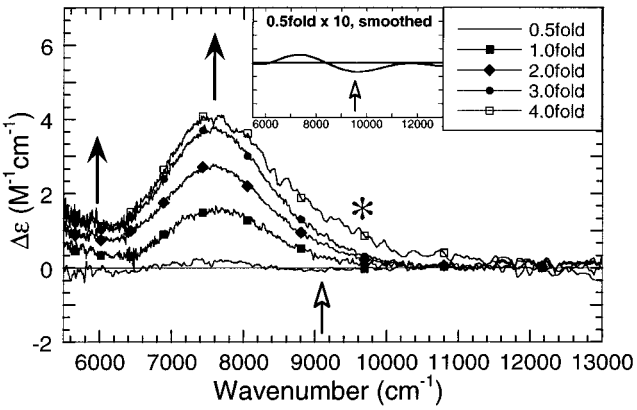


**Figure 3.** MCD spectra at 5 K, 7 T of apo RR in the presence of a 0.5 (—), 1.0 (■), 2.0 (◆), 3.0 (●), and 4.0 (□) molar equiv of ferrous ion. The 0.5-fold curve is smoothed and expanded 10 times in the inset.

Density functional calculations were performed on IBM 3BT-RS/6000 workstations using the Amsterdam Density Functional (ADF) program version 2.0.1 developed by Baerends et al.[52−54] The active site structures of reduced ribonucleotide reductase (reduced RR) and reduced $\Delta^9$-desaturase (reduced $\Delta^9$D) were approximated by models in which formates replace the carboxylates and amines replace the histidines. The coordinates were obtained from the Brookhaven Protein Data Bank (file 1XIK and 1AFR, respectively), averaged for the two subunits of each species, and adjusted to the more reasonable bond lengths associated with high-spin ferrous model complexes. The final coordinates of the corresponding atoms were then obtained by energy minimization with the distance between the two iron atoms kept frozen for comparison.

A triple-$\xi$ Slater-type orbital basis set (ADF basis set IV) with a single polarization function was used for each atom. Core orbitals were frozen through 1s (N, O) and 3p (Fe). All calculations were performed with the local density approximation of Vosko, Wilk, and Nusair[55] for the exchange and correlation energy and the nonlocal gradient corrections to exchange and correlation by Becke[56] and Perdew, respectively.[57] Geometries were optimized by using the algorithm of Versluis and Ziegler,[58] and changes in energy and coordinates between subsequent iterations were set to be below 0.01 hartrees/Å and 0.01 Å, respectively. Graphical output of the computational results was generated with the Cerius[2] software program developed by Molecular Simulations Inc.

## Results and Analysis

**1. Spectroscopy. A. $Fe^{II}$ Binding Titrations. (a) NIR CD.** Figure 2 shows the room-temperature CD titration of the apo form of R2 with ferrous ion in the NIR region from 5000 to 13000 $cm^{-1}$. The two binuclear active sites in the homodimer R2 subunits can, in principle, accommodate up to 4 iron atoms. R2 isolated in several laboratories and by several different procedures generally takes up 3.2−3.6 ferrous ions during complete reconstitution. Our protein is completely reconstituted after addition of 3.2 ferrous ions. The reason for the less-than-theoretical complement of $Fe^{II}$ sites is not known. In the presence of 0.5-fold equiv of ferrous ion, there are weak positive and weak negative transitions at about 7000 and 9700 $cm^{-1}$, respectively (Figure 2, inset). An additional positive transition clearly appears at about 5500 $cm^{-1}$ when the ferrous ion concentration is >1.0-fold equiv. These three transitions increase in intensity with increasing concentration of ferrous ion. The negative peak is saturated at ∼2 equiv of ferrous ion, while the two positive peaks do not saturate until >3 equiv of ferrous ion are added.[59] The presence of three transitions in the NIR region when the metal binding sites are fully loaded shows that the two irons in the active site are not equivalent. The presence of only one transition at an energy of >8000 $cm^{-1}$ indicates that neither iron is 6-coordinate and requires that one iron is 5-coordinate (FeB), which is inconsistent with the results of crystallography.[15] (To be consistent with the labeling used in the Mössbauer study,[51] FeB refers to this 5-coordinate iron that has a higher binding affinity (vide infra), and FeA to the other center.) The fact that the 9700-$cm^{-1}$ transition shows a concentration saturation behavior different from that of the two bands at 5500 and 7000 $cm^{-1}$ indicates that the latter are associated with the second iron (FeA). The fact that the ligand field transitions are below 8000 $cm^{-1}$ implies that this is a 4C center. Thus the two ferrous centers in the reduced active site are 4- and 5-coordinate. The titration in Figure 2 shows that the two iron sites have different metal binding affinities. The estimated[60] binding constants show that the 5C center binds ferrous ion at least ∼5-fold more tightly than the 4C center, which is consistent with the Mössbauer experiments.[51] On the basis of the ratio of their binding affinities, the relative occupancy of the 5C and 4C sites in the 0.5-fold iron adduct sample is approximately 80% and 20%, respectively.[61] Thus the FeB (5C)-bound mononuclear form is dominant at low equivalents of iron. The formation of the binuclear site via binding of FeA (4C) does not appear to significantly perturb the FeB (5C) center. This is consistent with the overall similarity in the crystal structures between the apo and the fully loaded reduced forms of the enzyme.[15,62]

**(b) NIR MCD.** Low-temperature MCD spectra were obtained for samples corresponding to the room-temperature CD titration of apo RR with $Fe^{II}$ (Figure 3). Two transitions are observed at about 5500 and 7500 $cm^{-1}$ corresponding to the two positive CD transitions (Figure 2). These two transitions increase in intensity upon increase in the equivalents of ferrous ion added and show a similar concentration saturation behavior. Thus they

(52) Baerends, E. J.; Ellis, D. E.; Ros, P. *Chem. Phys.* **1973**, *2*, 42.
(53) te Velde, G.; Baerends, E. J. *Int. J. Comput. Phys.* **1992**, *99*, 84.
(54) ADF 2.0.1 User's Guide; Theoretical Chemistry, Vrije Universiteit, The Netherlands.
(55) Vosko, S. H.; Wilk, L.; Nusair, M. *Can J. Phys.* **1980**, *58*, 1200.
(56) Becke, A. D. *J. Chem. Phys.* **1986**, *84*, 4524−4529.
(57) Perdew, J. P. *Phys. Rev. B* **1986**, *33*, 8822.
(58) Versluis, L.; Ziegler, T. *J. Chem. Phys.* **1988**, *88*, 322.

(59) This is consistent with the observation of 3−3.5 equiv of ferrous ion bound to the site in the purified protein and likely relate to ∼20% of the protein either being in a different conformation or in some other way damaged.
(60) Connors, K. A. *Binding Constants*; John Wiley & Sons: New York, 1987.
(61) The weak positive transition at 7000 $cm^{-1}$ in the 0.5-fold sample (Figure 2 inset) derives from the 20% occupancy of the 4C site.
(62) Åberg, A.; Nordlund, P.; Eklund, H. *Nature* **1993**, *361*, 276−278.

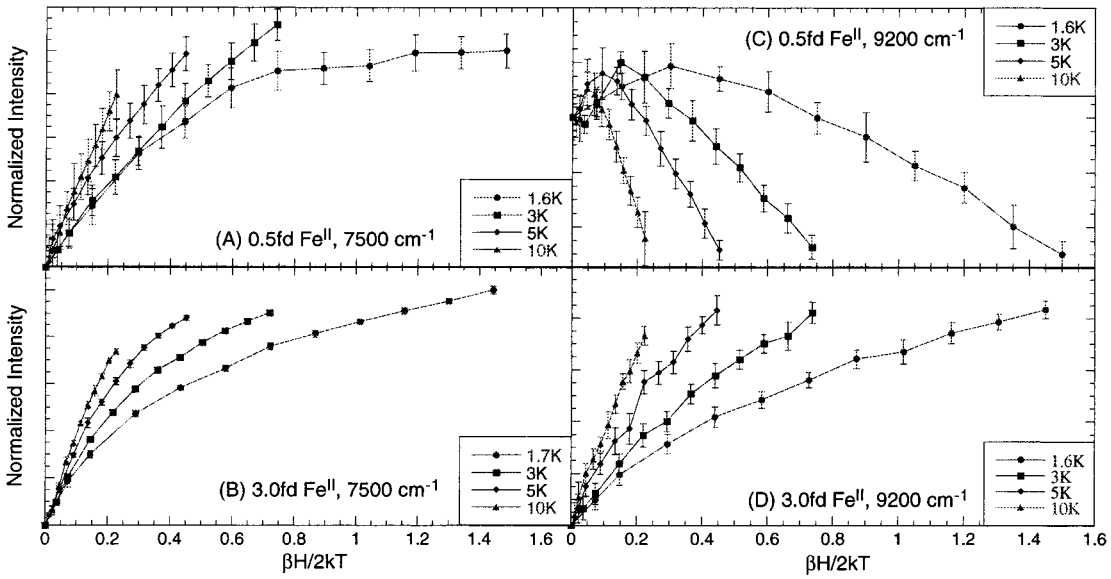


**Figure 4.** Saturation magnetization behavior of the MCD signal in the ligand field region for (A) 0.5-fold Fe$^{II}$-RR at 7500 cm$^{-1}$, (B) 3.0-fold Fe$^{II}$-RR at 7500 cm$^{-1}$, (C) 0.5-fold Fe$^{II}$-RR at 9200 cm$^{-1}$, and (D) 3.0-fold Fe$^{II}$-RR at 9200 cm$^{-1}$. The intensity amplitude (symbol) for a range of magnetic fields (0−7.0 T) at a series of fixed temperatures is plotted as a function of $\beta H/2kT$. Error bars are included.

can be correlated to the 4-coordinate iron (FeA). At low iron addition to apo RR (0.5-fold equiv), there is an additional weak negative transition at ∼9200 cm$^{-1}$ that can be associated with the 5-coordinate iron (FeB) (Figure 3 inset). On the basis of the results from the CD titration, the 5-coordinate site binds ferrous ion with a higher affinity than the 4-coordinate site, and at 0.5-fold equiv, approximately 20% of the adduct ferrous ion occupies the 4C center that has more intense MCD bands. At high equivalence (≥4.0-fold), a broad shoulder appears at the 9000-cm$^{-1}$ region, which can be associated with excess ferrous ion in solution. The 6-coordinate hexaaqua-ferrous complex shows two weak positive MCD transitions around 10000 cm$^{-1}$ (data not shown) and is not observed in the CD spectrum, as it is not chiral.

**(c) VTVH MCD.** The three MCD transitions described above all increase in signal intensity as temperature decreases, indicating that they are MCD ***C***-terms. Thus the ground state of reduced RR is a paramagnetic doublet that can split in energy in a magnetic field. It should be noted that two different forms are observed in the above CD/MCD titrations. At low equivalents of added iron (0.5-fold), the major species is a mononuclear active site with FeB (5C)-bound, while at high iron equivalents (>3.0-fold), both irons are bound and a binuclear active site consisting of the 5C and a 4C iron is obtained. Thus transitions associated with these two forms should give different saturation magnetization behaviors reflecting the different ground states of the monomer and the dimer. Variable-temperature variable-field (VTVH) MCD data were collected at 9200 and 7500 cm$^{-1}$ corresponding to the transitions for FeB (5C) and FeA (4C), respectively, as a function of concentration to probe the ground state of the individual iron sites. From the above results, the band associated with the 4C site should only reflect the coupled binuclear ground state, while the 5C transition can give mixed ground-state behavior with contributions from both the monomer and dimer based on the fact that at 0.5-fold equiv of iron the dimer already has 20% occupancy.

Figure 4 shows the saturation magnetization curves obtained at the two energies for different added equivalents of ferrous ion. The saturation curves for reduced RR do not superimpose, but are nested, with the high-temperature data offset from the low-temperature data when the isotherms are plotted as a function of $\beta H/2kT$. This is associated with rhombic zero-field splitting (ZFS) of a non-Kramers doublet ground state and arises from nonlinear field-induced mixing between the sublevels of the doublet. The VTVH MCD data collected at 7500 cm$^{-1}$ for the 0.5-, 1-, 2-, and 3-fold equiv of ferrous ion added to apo RR show very similar saturation behavior (Figure 4A,B, data for 1- and 2-fold samples are not shown). This indicates that the ground state for this transition is the same in the presence of different amounts of ferrous ion. Thus for all Fe$^{II}$ concentrations the 7500-cm$^{-1}$ band is associated with a ground state of a binuclear site. Alternatively, the VTVH MCD data collected at 9200 cm$^{-1}$ are dramatically different depending on the amount of ferrous ion present in the sample. At low concentration of ferrous ion (0.5-fold, Figure 4C), the VTVH MCD intensity increases at low magnetic field but rapidly decreases to negative intensity with increase in magnetic field. However, for high equivalents of ferrous ion (3.0-fold, Figure 4D), the MCD intensity at 1.6 K increases with an increase in magnetic field, exhibiting very similar behavior to that observed at 7500 cm$^{-1}$ (Figure 4A,B) associated with the binuclear site. The data in Figure 4C indicate the presence of a negative transition in the 9200-cm$^{-1}$ region that can be observed only at low equivalents of Fe$^{II}$ (0.5-fold). These observations are consistent with the results from the MCD titration and correspond to a mononuclear 5C Fe$^{II}$ center.

While the ground state of the monomer iron center cannot be analyzed due to the high noise of the very weak MCD signal (Figure 3 inset and Figure 4C) and the additional contribution from 20% dimer, VTVH MCD data for the binuclear form (Figure 4B) have been analyzed in ref 48. This analysis showed that that the two irons have different magnitudes of the ZFS with opposite signs: $D_A = +4.0 \pm 2.0$ cm$^{-1}$ and $D_B = -10.0 \pm 1.0$ cm$^{-1}$. The two irons are weakly antiferromagnetically coupled with exchange coupling constant, $J = -0.5 \pm 0.1$ cm$^{-1}$. This generates a ground sublevel with $M_s = \pm 2$ and an $M_s = \pm 1$ excited sublevel at $6.0 \pm 0.8$ cm$^{-1}$ above the ground state. The positive but relatively small ZFS is associated with the 4-coordinate site and the negative ZFS correlates to the 5-coordinate site. The electronic origin of the sign of the ZFS is considered in Section 2A.

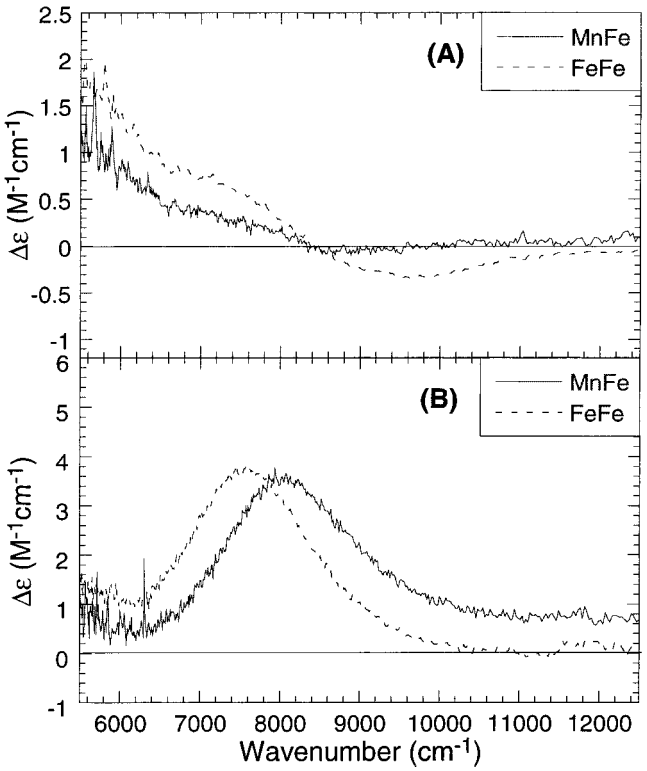


**Figure 5.** (A) CD and (B) LT MCD spectra of the binuclear $Fe^{II}Mn^{II}$ (—) and $Fe^{II}Fe^{II}$ (- - -) active sites in reduced RR. The CD and low-temperature MCD mixed-metal samples were prepared with 2.5-fold equiv of $Mn^{II}$ and 2.0-fold equiv of $Fe^{II}$ loaded apo RR. The spectra were recorded at 5 °C (CD) and 5 K, 7 T (MCD).

**B. Mixed Metal Derivative. (a) CD and MCD Measurements.** The difference in binding affinities of the two iron centers and the high affinity of the 5C site suggested that it might be possible to bind another metal to this site and prepare a mixed-metal derivative. Among the transition metals that do not exhibit intense ligand field transitions in the 5000−12000 $cm^{-1}$ region, $Mn^{II}$ has been found to bind to apo RR tightly.[63] Thus 2.5-fold equiv of $Mn^{II}$ was added to apo RR. The UV−vis absorption spectrum exhibited no signal associated with manganese. On the basis of the fact that $Mn^{III}$ exhibits spin-allowed ligand field transitions in the UV−vis region,[64] this result indicates that only $Mn^{II}$ is present. A CD titration of this Mn-containing sample was performed by adding increasing equivalents of ferrous ion. Two positive transitions at 5500 and 7200 $cm^{-1}$ appear with increase in concentration of ferrous ion and saturate at 1.5-fold equiv (Figure 5A, the solid line is the final product of the titration with 2.5-fold $Mn^{II}$ and 2-fold $Fe^{II}$ present). The negative transition at 9700 $cm^{-1}$ of the binuclear ferrous site (Figure 2 and dashed line in Figure 5B**)** is no longer present. The absence of the 9700-$cm^{-1}$ transition in MnFe derivative, which is associated with the 5C site in the all-Fe form, suggests that $Mn^{II}$ selectively occupies the 5C metal binding site that also has a higher binding affinity for $Fe^{II}$. The two bands at 5500 and 7200 $cm^{-1}$ in the MnFe derivative are also present in the all-Fe occupied form and can be correlated with the 4C site that also has a lower $Fe^{II}$ binding affinity. Thus $Mn^{II}$ occupies the 5C site at low equivalents and additional $Fe^{II}$ then occupies the 4C site demonstrating that the mixed-metal derivative has been obtained (MnFe-RR). The CD spectrum of this dimer confirms the assignment of the high-energy transition at 9700 $cm^{-1}$ to the 5-coordinate site and the other two transitions to the 4C site, consistent with the results obtained above for the all-Fe occupied form.

(63) Atta, M.; Nordlund, P.; Åberg, A.; Eklund, H.; Fontecave, M. *J. Biol. Chem.* **1992**, *267*, 20682−20688.

(64) Brunold, T. C.; Gamelin, D. R.; Stemmler, T. L.; Mandal, S. K.; Armstrong, W. H.; Pannerhahn, J. E.; Solomon, E. I. *J. Am. Chem. Soc.* **1998**, *120*, 8724−8738.

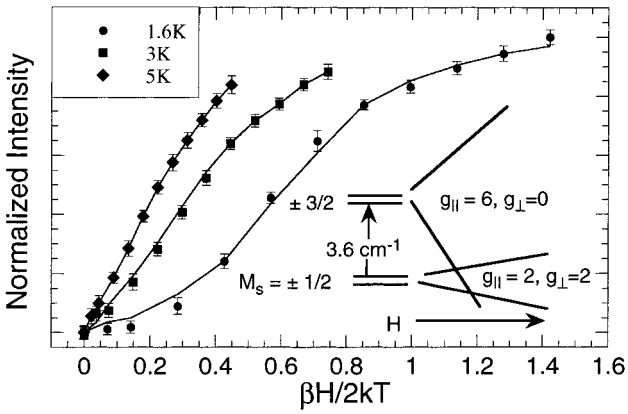


**Figure 6.** Saturation magnetization behavior of the MCD signal in the ligand field region at 8000 $cm^{-1}$ for the binuclear $Fe^{II}Mn^{II}$ site in reduced RR. The intensity amplitude (symbol) for a range of magnetic fields (0−7.0 T) at a series of fixed temperatures is plotted as a function of $\beta H/2kT$. Error bars are included. The fit to the VTVH MCD data (solid line) was obtained using a Kramers doublet model. The parameters are given in Table 1 and the resultant energy level diagram is presented in the inset.

The MCD spectrum for MnFe-RR is given in Figure 5B, solid line. One positive transition is observed at ∼8000 $cm^{-1}$. This MCD spectrum is similar to that of Fe-RR (Figure 5B, dash line). The transition at 7500 $cm^{-1}$ has shifted up in energy by ∼500 $cm^{-1}$ and the lower energy transition at 5500 $cm^{-1}$ appears to have decreased in intensity. These minor changes indicate that the ligand field of the 4C $Fe^{II}$ is not dramatically altered upon the substitution of Mn for Fe at the 5C site.

**(b) VTVH MCD and Ground-State Analysis.** VTVH MCD data were collected at the 8000 $cm^{-1}$ band to probe the ground state of MnFe-RR (Figure 6, symbols with the standard deviation are shown as an error bar for each datum point). The active site has $S = 2$ ($Fe^{II}$) and $S = {}^5/_2$ ($Mn^{II}$) ions antiferromagnetically coupled to give an $S_{tot} = {}^1/_2$ Kramers ground state. The variable-field saturation curves obtained at fixed increasing temperatures when plotted as a function of $\beta H/2kT$ do not superimpose, but are nested, which for a Kramers system is associated with the population of excited states. The change of slope observed in the low-temperature low-field data suggests the possibility of a ground-state crossover with magnetic field due to the presence of a low-lying excited state. The VTVH MCD data were fit using the MCD intensity expression for a Kramers system which allows for the effects of a linear ***B***-term (from field-induced mixing with higher energy states), eq 1:[65−69]

$$\Delta\epsilon = \sum_i \left[ (A_{\text{sat lim}})_i \left( \int_0^{\pi/2} \frac{\cos^2\theta \sin\theta}{\Gamma_i} g_{\|i}\, \beta H \alpha_i \, d\theta - \sqrt{2}\frac{M_z}{M_{xy}} \int_0^{\pi/2} \frac{\sin^3\theta}{\Gamma_i} g_{\perp i}\, \beta H \alpha_i \, d\theta \right) + B_i H \gamma_i \right] \quad (1)$$

where

$$\Gamma_i = \sqrt{(g_{\|i}\, \beta H \cos\theta)^2 + (g_{\perp i}\, \beta H \sin\theta)^2}$$

$$\alpha_i = \frac{e^{-(E_i-\Gamma_i/2)/kT} - e^{-(E_i+\Gamma_i/2)/kT}}{\sum_j e^{-(E_j-\Gamma_j/2)/kT} + e^{-(E_j+\Gamma_j/2)/kT}}$$

$$\gamma_i = \frac{e^{-(E_i)/kT}}{\sum_j e^{-(E_j)/kT}}$$

$(A_{\mathrm{sat\ lim}})_i$, $B_i$, $g_{\|i}$, and $g_{\perp i}$ are the ***C***-term and ***B***-term MCD intensity, and the dimer effective *g*-values of the *i*th doublet, respectively. $E_i$ is the energy of the *i*th sublevel, and the factors $\alpha_i$ and $\gamma_i$ are the Boltzmann populations for the ***C***-term and ***B***-term, respectively. $H$ is the applied magnetic field, $\beta$ is the Bohr magneton, $k$ is the Boltzmann constant, $T$ is the absolute temperature, and $M_z$ and $M_{xy}$ are the transition dipole moments for the direction indicated. Different combinations of these parameters lead to different VTVH MCD behaviors. The detailed methodology for VTVH MCD analysis for Kramers systems of this type of dimer has been presented in ref 70. Using eq 2 to fit the data in Figure 6 indicates that the ground state is $S_{\mathrm{tot}} = {}^1/_2$, $M_s = \pm{}^1/_2$ and an $S_{\mathrm{tot}} = {}^3/_2$, $M_s = \pm{}^3/_2$ excited state is at 3.6 $\mathrm{cm}^{-1}$ above the ground state. These two $M_s$ sublevels split in the presence of a magnetic field and cross over due to the low energy of the excited state (Figure 6 inset). Table 1 summarizes the best fit to the VTVH MCD data.

A spin-Hamiltonian analysis was further performed to interpret the excited-state energies and *g* values obtained from the VTVH MCD fit. Equation 2 presents the spin-Hamiltonian for an [$Fe^{II}Mn^{II}$] system including the combined effects of single-site zero-field splitting and the exchange coupling interaction between the two metals through the bridging ligands.

$$\begin{aligned} H = {} & -2JS_{\mathrm{Fe^{II}}}S_{\mathrm{Mn^{II}}} + D_{\mathrm{Fe^{II}}}(S^2_{\mathrm{zFe^{II}}} - 2) + E_{\mathrm{Fe^{II}}}(S^2_{\mathrm{xFe^{II}}} - \\ & S^2_{\mathrm{yFe^{II}}}) + D_{\mathrm{Mn^{II}}}(S^2_{\mathrm{zMn^{II}}} - 35/12) + g_{\mathrm{zFe^{II}}}\beta H_z S_{\mathrm{zFe^{II}}} + \\ & g_{\mathrm{xFe^{II}}}\beta H_x S_{\mathrm{xFe^{II}}} + g_{\mathrm{yFe^{II}}}\beta H_y S_{\mathrm{yFe^{II}}} + g_{\mathrm{zMn^{II}}}\beta H_z S_{\mathrm{zMn^{II}}} + \\ & g_{\mathrm{xMn^{II}}}\beta H_x S_{\mathrm{xMn^{II}}} + g_{\mathrm{yMn^{II}}}\beta H_y S_{\mathrm{yMn^{II}}} \quad (2) \end{aligned}$$

with

$$D_{\mathrm{Fe^{II}}} = (-k^2\lambda_0/4)(g_{\mathrm{xFe^{II}}} + g_{\mathrm{yFe^{II}}} - 2g_{\mathrm{zFe^{II}}}) \quad (3a)$$

$$E_{\mathrm{Fe^{II}}} = (-k^2\lambda_0/4)(g_{\mathrm{yFe^{II}}} - g_{\mathrm{xFe^{II}}}) \quad (3b)$$

Included in eq 2 are the exchange coupling constant $J$, the axial ($D_{\mathrm{Fe^{II}}}$, $D_{\mathrm{Mn^{II}}}$) and rhombic ($E_{\mathrm{Fe^{II}}}$) zero field splitting (ZFS), and the Zeeman effect ($g_{\mathrm{ZFe^{II}}}\beta H_Z S_{\mathrm{ZFe^{II}}}$, etc). The single site $g_i$ value for an $Fe^{II}$ can be related to the ZFS parameters using ligand field theory as given in eqs 3a and 3b, in which $\lambda_0$ is the $Fe^{II}$ ground-state spin−orbit coupling constant (~100 $\mathrm{cm}^{-1}$) and $k^2$ is the Stevens orbital reduction factor which is <1 due to convalency. In this analysis, the ZFS of $Mn^{II}$ was constrained to be axial with a $D$ value less than 1 $\mathrm{cm}^{-1}$. Table 2 gives the ground-state parameters for MnFe-RR. The corresponding parameters for reduced all-Fe RR are included for comparison.

**Table 1.** VTVH MCD Parameters for the Ground State and Lowest Excited States of Binuclear [$Mn^{II}Fe^{II}$] Ribonucleotide Reductase

| | VTVH MCD (8000 $\mathrm{cm}^{-1}$) | | | | | |
|---|---|---|---|---|---|---|
| | $A_{\mathrm{sat}}$ | $B$ (% of $A_{\mathrm{sat}}$) | $g_{\|\|}$ | $g_\perp$ | $M_z/M_x$ | $E$ ($\mathrm{cm}^{-1}$) |
| G.S. | 6.24 | 0.8263 | 2.00 | 2.00 | 0.53 | 0.00 |
| E.S. | 3.22 | 0.9787 | 6.00 | 0.00 | 0.53 | 3.62 |

The above analysis utilizes ***B***-term contributions to MCD intensity to represent the second-order Zeeman interactions between levels. The VTVH MCD intensity was also simulated using the dimer wave functions from eq 2 and the fact that the MCD intensity is proportional to the spin-expectation values of the single iron center being studied by MCD projected onto the dimer states.[71] Simulations were performed over a series of $D_{\mathrm{A}}(4\mathrm{C,Fe^{II}})$, $D_{\mathrm{B}}(5\mathrm{C,Mn^{II}})$, and $J$ values using a wide range of the effective transition moment products $M_{xy}$, $M_{xz}$, and $M_{yx}$. The results indicate that good agreement with the VTVH MCD data shown in Figure 6 is achieved with $D_{\mathrm{A}}(4\mathrm{C,Fe^{II}}) = +6.0\ \mathrm{cm}^{-1}$, $D_{\mathrm{B}}(5\mathrm{C,Mn^{II}}) = -0.8\ \mathrm{cm}^{-1}$, and $-J = \sim 0.6\ \mathrm{cm}^{-1}$ (simulation curves are given in the Supporting Information). These ground-state parameters are similar to those obtained from the spin-Hamiltonian analysis of the VTVH MCD fit using eq 2 (Table 2).

In summary, the results show that the two metal centers remain weakly antiferromagnetically coupled upon the $Mn^{II}$ substitution, indicating the presence of a similar bridging environment between the two metals. The magnitude and sign of the ZFS for the $Fe^{II}$ center in MnFe-RR is consistent with that of the 4C site in the all-Fe RR.

**C. Chemical Perturbation.** The $Fe^{II}$ binding and mixed-metal derivative studies described above suggest that the active site of reduced RR consists of one 5- and one 4-coordinate iron center. This model, however, is not consistent with the active site structure determined crystallographically which has two 4C sites. Conditions used for crystallization and data collection were very different from those employed in this study. The room-temperature CD spectra of reduced RR were prepared at pH7.6 and 4 °C; the low-temperature MCD samples of reduced RR were prepared at pH 7.6 and 5 K with 60% glycerol, while the crystal structure was obtained at pH 5−6 in the presence of 0.2 M NaCl and polyethelene glycol 4000.[15] To investigate the discrepancy between the results obtained at two different conditions, a series of CD experiments were performed with the conditions varied between those used for MCD and crystallography. The CD spectra remain unchanged upon addition of 60% glycerol and decrease of temperature to 5 K. A dramatic perturbation was not found upon decreasing the pH to 6.5. A pH 8.0 sample was then used to investigate the effect of addition of 0.2 M NaCl. A slight amount of precipitation was observed during incubation. The NIR CD spectrum of the supernatant is shown in Figure 7A (curve with solid triangles). Compared to the CD spectrum for the pH 8.0 sample without NaCl (Figure 7A, curve with solid circles), the results show a decrease in the intensities of the two low-energy transitions at 5500 and 7000 $\mathrm{cm}^{-1}$ associated with the 4C center. A larger change was observed in the higher energy region. The transition at 9500 $\mathrm{cm}^{-1}$ associated with the 5C site was replaced by two transitions: one weak negative and one weak positive peak at about 8500 and 10500 $\mathrm{cm}^{-1}$, respectively. This suggests that the addition of chloride significantly affects both the 4C and

(65) Zhang, Y.; Gebhard, M. S.; Solomon, E. I. *J. Am. Chem. Soc.* **1991**, *113*, 5162−5175.
(66) Solomon, E. I.; Pavel, E. G.; Loeb, K. E.; Campochiaro, C. *Coord. Chem. Rev.* **1995**, *144*, 369−460.
(67) Stevens, P. J. *Annu. Rev. Phys. Chem.* **1974**, *25*, 201.
(68) Bennett, D. E.; Johnson, M. K. *Biochim. Biophys. Acta* **1987**, *911*, 71−80.
(69) Schatz, P. N.; Mowery, R. L.; Krausz, E. R. *Mol. Phys.* **1978**, *35*, 1537−1557.
(70) Yang, Y.-S.; McCormick, J. M.; Solomon, E. I. *J. Am. Chem. Soc.* **1997**, *119*, 11832−11842.
(71) Neese, F.; Solomon, E. I. *Inorg. Chem.* **1999**, *38*, 1847−1865.

**Table 2.** Spin Hamiltonian Parameters for Binuclear [$Mn^{II}Fe^{II}$] and [$Fe^{II}Fe^{II}$] Ribonucleotide Reductase

| | ground-state parameters ($cm^{-1}$) | | | |
|---|---|---|---|---|
| | $J$ | $D_B$(5C) | $D_A$(4C) | $E_A$(4C) |
| MnFe-RR | $-1.2 \pm 0.4$ | $-0.82 \pm 0.2$ ($Mn^{II}$) | $+3.2 \pm 0.7$ ($Fe^{II}$) | $0.22 \pm 0.5$ |
| reduced RR | $-0.5 \pm 0.2$ | $-10.0 \pm 5.0$ ($Fe^{II}$) | $+5.0 \pm 3.0$ ($Fe^{II}$) | – |

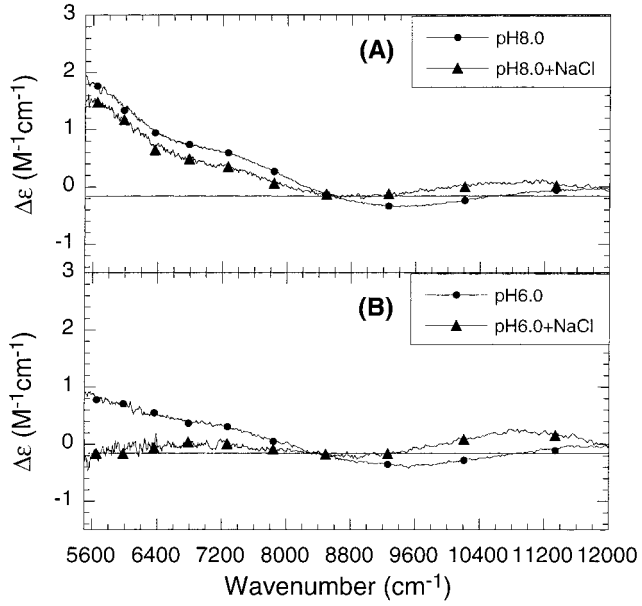


**Figure 7.** (A) CD spectra at 5 °C of 3.0-fold $Fe^{II}$-RR at pH 8.0 without (●) and with (▲) the addition of 0.2 M NaCl. (B) CD spectra at 5 °C of 3.0-fold $Fe^{II}$-RR at pH 6.0 without (●) and with (▲) the addition of 0.2 M NaCl.

5C sites, which is also observed in the corresponding MCD spectrum (Supporting Information).

A significant amount of precipitation was observed as the pH was decreased below 6.5. At pH 6.0 about 50% of the sample is still found in the supernatant. Upon addition of 0.2 M NaCl the precipitation further increased. Further lowering of the pH to approximate the crystallographic conditions led to extensive precipitate. The effect of salt on the CD spectrum of the supernatant at pH 6.0 is shown in Figure 7B. The positive transitions in the low-energy region associated with the 4C site are eliminated with 0.2 M NaCl (curve with solid triangles). One negative peak and one positive peak appear around 10000 $cm^{-1}$, which is similar to the behavior observed for the CD spectrum at pH 8.0 with 0.2 M NaCl (Figure 7A, curve with solid triangles). Reproducible data could not be obtained at pH <6.0 due to extensive precipitation. Thus both pH and salt perturb the active site of reduced RR; however, the results in Figure 7 do not correlate with the crystal structure. To further pursue this issue, spectroscopic data on the protein crystals are required.

**2. Electronic Structure Calculations.** CD/MCD/VTVH MCD studies on the reduced sites of RR and $\Delta^9$D have been reported in which the ligand field spectral features for both enzymes have been defined.[39,48] The spectral data for reduced $\Delta^9$D are in good agreement with the X-ray structure.[16] The spectral data for reduced RR indicate that the active site consists of one 5C- and one 4C-iron center, while under crystallographic conditions the site contains two 4C-iron centers.[15] Here a series of density functional calculations are presented on reduced RR and reduced $\Delta^9$D to correlate to the spectral features and gain insight into the electronic structures of these reduced sites. These protein sites show large differences in dioxygen reactivity and the origin of these differences is considered through the interaction of these experimentally calibrated electronic structures with dioxygen. Note that neither protons nor solvent molecules were included in the calculations. No proton is required or appears to participate in the reaction of reduced RR and reduced $\Delta^9$D with $O_2$ to generate peroxo species, and no solvent molecule is observed close to the active sites in the crystal structures.[15,16]

**A. Reduced Ribonucleotide Reductase.** Figure 1B shows the initial structure used for the active site of reduced RR that was obtained from the PDB file. The bond lengths were averaged over the two subunits and modified to be within the range found for binuclear ferrous model complexes.[72−79] On the basis of the facts that (1) spectroscopic results indicate that the active site contains one 4C and one 5C iron center at pH 7.6 in solution and (2) in the crystal structure the Glu204 is disordered,[15] the distance between FeB and the unbound oxygen atom of Glu204 was shortened to be within possible bonding distance (2.4 Å).[80] The modified active site structure was then energy minimized to obtain an optimal structure (Figure 8A, final coordinates are given in the Supporting Information). The optimized structure has Fe−O bond lengths between 2.10 and 2.21 Å and Fe−N bond lengths of 2.16 and 2.17 Å. The active site has one 5- and one 4-coordinate iron consistent with the CD/MCD results.[48]

Density functional calculations on the optimized reduced RR structure were performed both for the ferromagnetic high-spin (HS, $S_{tot} = 4$, $M_s = 4$) and the broken symmetry (BS, $M_s = 0$) ground state. The total binding energy,[81] $E_{tot}$, of the BS calculation is −156.51 eV. The energy level diagram obtained from the BS calculation is shown in Figure 9. Each ferrous ion is localized and has four unoccupied and one occupied d-based orbitals of one spin and another 5 occupied levels with the opposite spin that are greatly stabilized in energy. The relative energies and compositions of the relevant FeB (5C) and FeA (4C) d-based molecular orbitals (MOs) are given in Table 3. The local axes shown in Figure 8A indicate the principal

(72) Chauduri, P.; Wieghardt, K. *Angew. Chem., Int. Ed. Engl.* **1985**, *24*, 778.
(73) Hartman, J. R.; Rardin, R. L.; Chauduri, P.; Pohl, K.; Weighardt, K.; Nuber, B.; Weiss, J.; Papaefthymiou, G. C.; Frankel, R. B.; Lippard, S. J. *J. Am. Chem. Soc.* **1987**, *109*, 7387.
(74) Hagen, K. S.; Lachicotte, R. *J. Am. Chem. Soc.* **1992**, *114*, 8741−8742.
(75) Hendrich, M. P.; Day, E. P.; Wang, C.-P.; Synder, B. S.; Holm, R. H.; Münck, E. *Inorg. Chem.* **1994**, *33*, 2848−2856.
(76) Kitajima, N.; Tamura, N.; Tanaka, M.; Moro-oka, Y. *Inorg. Chem.* **1992**, *31*, 3342−3343.
(77) Herold, S.; Lippard, S. J. *J. Am. Chem. Soc.* **1997**, *119*, 145−156.
(78) Tolman, W. B.; Liu, S.; Bentsen, J. G.; Lippard, S. J. *J. Am. Chem. Soc.* **1991**, *113*, 152−164.
(79) Lee, D.; Lippard, S. J. *J. Am. Chem. Soc.* **1998**, *120*, 12153−12154.
(80) Geometry-optimized calculations performed on an active site with two 4C sites based on the crystal structure showed a higher $E_{tot}$ (∼0.8 eV) compared to that of the 4C+5C sites from spectroscopy. Calculations of the total energy differences between the ground and excited states showed that the 4C Fe site in both the 4C+5C and 4C+4C structures has similar ligand field transition energies. However, the ligand field transitions are about 3000 $cm^{-1}$ higher in energy in the 5C site relative to the second 4C site in the 4C+4C structure, where only the former is consistent with the experimentally observed ligand field transition energies.
(81) Total binding energy of a system is defined relative to the isolated atom fragments.

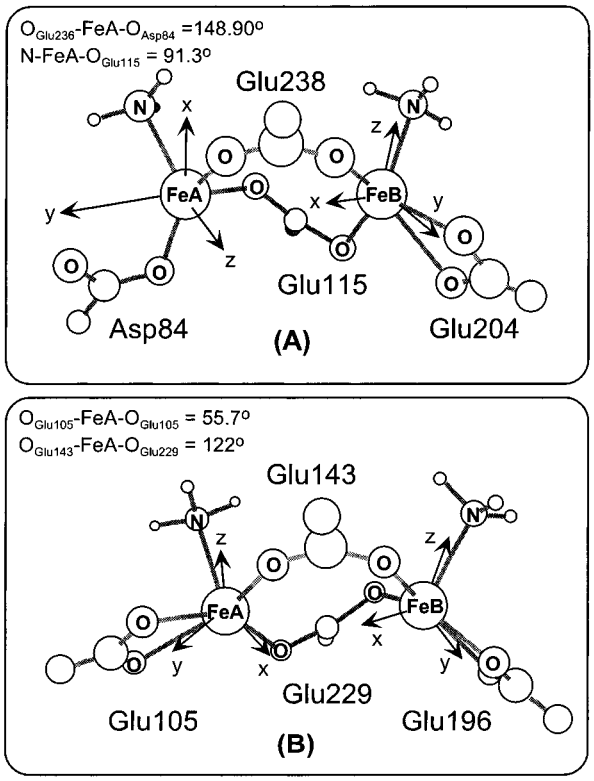


**Figure 8.** Energy minimized binuclear active site structures of (A) reduced RR and (B) reduced $\Delta^9$D. The axes indicated are the principal directions of the single site *D* tensors. The *z*-axis of FeA in reduced RR approximately bisects the wide $O_{Glu238}$*−Fe−$O_{Asp84}$* angle, and the *z*-axes of FeB in reduced RR and the two Fe centers in reduced $\Delta^9$D are along the Fe−N bonds. Key structural features are listed in the inset of the figure.

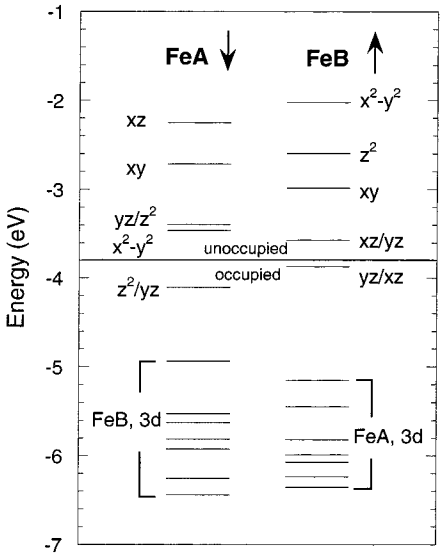


**Figure 9.** Energy level diagram obtained from a BS calculation on reduced RR (Figure 8A). The orbitals are labeled based on their major composition (Table 3). The arrows indicate orbital spin.

directions of the *D* tensors (vide infra). The *z*-axis of the 4C site approximately bisects the wide $O_{Glu238}$−FeA−$O_{Asp84}$ angle (148.9°), and the *z*-axis of the 5C site is along the Fe−N bond. The splitting pattern in Figure 9 of the quintet ligand field states of FeB (5C) is typical for a distorted square-pyramidal geometry. In the ground state, the extra electron of FeB occupies the *yz*/*xz*-based spin-up MO. (Throughout this study we will use an abbreviated notation for d orbitals, e.g., *yz* standing for $d_{yz}$.) The splitting pattern of the five d-based spin-down MOs of FeA (4C) is consistent with a $C_{2v}$ distorted tetrahedral geometry (Figure 8A, ∠$O_{Glu238}$−FeA−$O_{Asp84}$ = 148.9° and ∠N−FeA−$O_{Glu115}$ = 91.3°) with the extra electron in a ground state with mixed $z^2$ and *yz* character (Table 3).

**Table 3.** Relative Energies, $E_{rel}$ (eV), and Compositions (%) of the Relevant Fe d-Based MOs Obtined from a BS Calculation for Reduced RR

| Spin-Up MO, Localized at FeB (5C) | | | | | | | | | |
|---|---|---|---|---|---|---|---|---|---|
| | | FeB | | | | | | | |
| level | $E_{rel}$ (eV) | *yz* | *xz* | *xy* | $x^2-y^2$ | $z^2$ | total | FeA | $Glu_{bridge}$ |
| | | | | unoccupied | | | | | |
| 54 | 1.845 | 8 | 2 | 4 | 60 | 8 | 82 | 0 | 7 |
| 53 | 1.273 | 1 | 2 | 38 | 10 | 25 | 76 | 1 | 4 |
| 52 | 0.886 | 2 | 3 | 33 | 1 | 39 | 78 | 0 | 4 |
| 51 | 0.297 | 24 | 54 | 2 | 7 | 0 | 87 | 1 | 4 |
| | | | | occupied | | | | | |
| 50 | 0.000 | 52 | 19 | 4 | 5 | 0 | 80 | 0 | 4 |
| Spin-Down MO, Localized at FeA (4C) | | | | | | | | | |
| | | FeA | | | | | | | |
| level | $E_{rel}$ (eV) | *yz* | *xz* | *xy* | $x^2-y^2$ | $z^2$ | total | FeB | $Glu_{bridge}$ |
| | | | | unoccupied | | | | | |
| 54 | 1.854 | 9 | 45 | 9 | 5 | 13 | 81 | 0 | 2 |
| 53 | 1.390 | 16 | 13 | 34 | 0 | 2 | 65 | 0 | 4 |
| 52 | 0.712 | 27 | 11 | 9 | 2 | 20 | 69 | 0 | 4 |
| 51 | 0.643 | 7 | 3 | 0 | 78 | 0 | 88 | 2 | 7 |
| | | | | occupied | | | | | |
| 50 | 0.000 | 27 | 6 | 13 | 5 | 45 | 96 | 0 | 4 |

**Table 4.** Comparison of the Calculated Ground State Parameters to the Experimental Values for Reduced RR

| | exp | | calcd | |
|---|---|---|---|---|
| | FeB (5C) | FeA (4C) | FeB (5C) | FeA (4C) |
| $J$ ($cm^{-1}$) | −0.5 | | +12.8 | |
| $D$ ($cm^{-1}$) | $-10 \pm 5$ | $+5 \pm 3$ | −3.80 | +0.85 |
| $\|E/D\|$ | | | 0.25 | 0.33 |

The computational results were evaluated based on the spectroscopic data. (1) The formalism developed by Noodleman was utilized to estimate the ground-state exchange coupling constant *J* from the difference in total energy between the HS ($M_s = 4$) and BS ($M_s = 0$) states, eq 4:[82]

$$J = -(E_{HS} - E_{BS})/S^2_{max} \quad (4)$$

The calculated total binding energies of HS and BS states give a value of $J = +12$ $cm^{-1}$. While the sign of *J* is not consistent with the experimental value (Table 4),[48] the magnitude of the exchange coupling is small, consistent with the experimental result that the two iron centers are weakly coupled. This reflects a poor superexchange pathway as demonstrated by the low composition of bridging carboxylate orbitals in the d-based levels (levels 50 to 54, Table 3). (2) The energies of the spin-allowed ligand field transitions of each Fe were calculated from the differences in total bonding energies of the ground and excited states at convergence. Table 5 compares the transition energies obtained from the CD/MCD studies with the calculations.[48] The results show that the calculated transition energies are somewhat higher than those obtained experimentally, indicating too large a ligand field energy splitting of the d orbitals in the calculations. This is likely due to differences in

(82) Noodleman, L. *J. Chem. Phys.* **1981**, *74*, 5737.

**Table 5.** Comparison of the Calculated Ligand Field Transition Energies to the Experimental Values for Reduced RR

| | FeB (5C) | | | FeA (4C) | |
|---|---|---|---|---|---|
| level | exp | calcd | level | exp | calcd |
| $x^2 - y^2$ | 9500 | 11000 | $xz$ | 7500 | 9900 |
| $z^2/xy$ | | 5000 | $xy$ | 5500 | 6500 |
| $xy/z^2$ | | 3300 | $yz/z^2$ | | 5900 |
| $xz$ | | 2900 | $x^2 - y^2$ | | 720 |
| $yz$ | | 0 | $z^2/yz$ | | 0 |

bond lengths between the protein site and the optimized structure. (3) The formalism developed in ref 83 was utilized to estimate the single site matrix elements of the *D* tensor from the calculated MO compositions and the energies of the ligand field transitions. The principal axis of the *D* tensor of each iron (Figure 8) was obtained by diagonalizing the corresponding matrix with the coordinate transformation defining the local coordinate system. Table 4 gives a comparison of the calculated ZFS parameters and those obtained from VTVH MCD and spin-Hamiltonian analysis.[48] The calculated ZFS of the 5C site is negative, which is consistent with experimental results and the distorted square-pyramidal geometry. The 4C site has $E/D = 0.33$, indicating that this site is very rhombic and thus that there would be no effect of the sign of *D* for a single Fe center. However, in the dimer the relative orientation of the *D* tensors of the two irons is dependent on the sign of *D*, which will make the energy splitting patterns different for different directions of the applied magnetic field. Thus the sign of *D* for the 4C site was chosen to be positive based on the experimental energy splitting of the ground sublevels obtained from VTVH MCD and spin-Hamiltonian analysis (Table 2).[48] The resultant *D* tensor has a principal *z*-axis approximately bisecting the $O_{Glu238}-FeA-O_{Asp84}$ angle as shown in Figure 8A. It should be noted that the magnitudes of both ZFSs are smaller than the experimental estimate. This reflects the fact that the major contributions to the ZFSs originate from spin−orbit coupling of the ground state to the ligand field excited states which are calculated at higher energy than that determined experimentally (Table 5).

The calculated excited-state energies and ZFS parameters obtained above for reduced RR result in an active site consisting of one 5C center with a distorted square-pyramidal geometry (*z* axis is along the Fe−N bond) and one 4C center with a $C_{2v}$ distorted tetrahedral geometry (Figure 8A, the $C_2$ axis bisects the $\angle O_{Glu238}-Fe-O_{Asp84}$ of FeA). The redox active orbitals are the *yz*- and $z^2/yz$-based MOs for the 5C (FeB) and the 4C (FeA) sites, respectively, shown in Figure 10A. In addition, from Table 5, each iron has an excited state (*xz* for FeB and $x^2 - y^2$ for FeA) that is low in energy (2900 and 720 $cm^{-1}$, respectively) and thus can also participate in reaction with dioxygen.

**B. Reduced $\Delta^9$ Desaturase.** The active site structure of reduced $\Delta^9$D used for the calculations was obtained from the PDB file (Figure 1C) and energy minimized. Figure 8B shows the optimized structure with the principal axes of the *D* tensors (vide infra). All the Fe−ligand bond lengths are within the range of those observed in binuclear ferrous model complexes (final coordinates are given in the Supporting Information).[72−79] The Fe−O bond lengths are between 2.01 and 2.20 Å, and the Fe−N bonds are 2.18 and 2.21 Å. The two iron sites are approximately equivalent with 5-coordinate distorted square-pyramidal geometries. The z-axes for both iron centers (principal axis for the ZFS *D* tensor, vide infra) are along the Fe−N(His) bonds.

(83) Neese, F.; Solomon, E. I. *Inorg. Chem.* **1998**, *37*, 6568−6582.

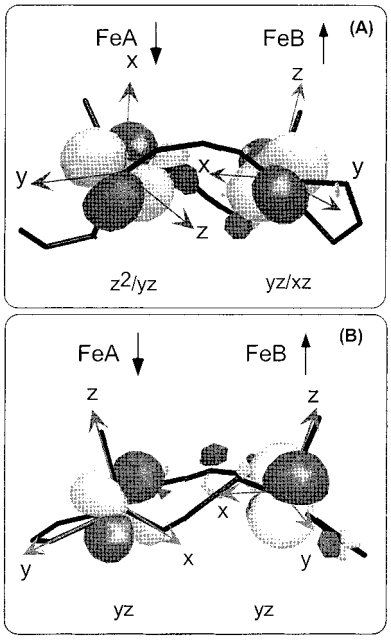


**Figure 10.** Surface plots of the redox active orbitals containing the extra (spin-up) electron of FeB and the extra (spin-down) electron of FeA, obtained from a BS ($M_s = 0$) calculation on (A) reduced RR and (B) reduced $\Delta^9$D. The axes indicated are the principal directions of the single site *D* tensors.

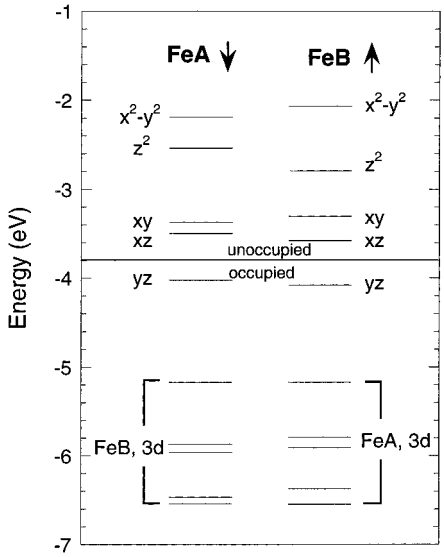


**Figure 11.** Energy level diagram obtained from a BS calculation on reduced $\Delta^9$D (Figure 8B). The orbitals are labeled based on their major composition (Table 6). The arrows indicate the orbital spin.

Calculations on the optimized structure of reduced $\Delta^9$D were performed for the ferromagnetic high-spin (HS, $M_s = 4$) and the broken symmetry (BS, $M_s = 0$) ground states. The $E_{tot}$ for the BS calculation is −157.72 eV. Each ferrous center is again localized with four unoccupied and one occupied d-based orbitals of one spin, and another five occupied orbitals of the opposite spin greatly stabilized in energy (Figure 11). The energies and compositions of the relevant FeB and FeA d-based molecular orbitals (MOs) are given in Table 6. The splitting patterns of the 5 ligand field states for both iron centers are typical for a distorted square-pyramidal geometry (Figure 11). The extra electrons of both irons occupy the *yz*-based MOs similar to the 5C center of reduced RR (vide infra).

**Table 6.** Relative Energies, $E_{rel}$ (eV), and Compositions (%) of the Relevant Fe d-Based MOs Obtained from a BS Calculation for Reduced $\Delta^9$D

| Spin-Up MO, Loclaized at FeB | | | | | | | | | |
|---|---|---|---|---|---|---|---|---|---|
| | | FeB | | | | | | | |
| level | $E_{rel}$ (eV) | *yz* | *xz* | *xy* | $x^2-y^2$ | $z^2$ | total | FeA | $Glu_{bridge}$ |
| | | | | unoccupied | | | | | |
| 54 | 2.015 | 13 | 2 | 8 | 55 | 11 | 83 | 0 | 3 |
| 53 | 1.288 | 0 | 6 | 29 | 20 | 29 | 84 | 0 | 3 |
| 52 | 0.776 | 0 | 2 | 42 | 0 | 34 | 78 | 0 | 2 |
| 51 | 0.503 | 1 | 81 | 0 | 9 | 4 | 95 | 0 | 3 |
| | | | | occupied | | | | | |
| 50 | 0.000 | 77 | 2 | 0 | 7 | 4 | 90 | 0 | 2 |
| Spin-Down MO, Localized at FeA | | | | | | | | | |
| | | FeA | | | | | | | |
| level | $E_{rel}$ (eV) | *yz* | *xz* | *xy* | $x^2-y^2$ | $z^2$ | total | FeB | $Glu_{bridge}$ |
| | | | | unoccupied | | | | | |
| 54 | 1.839 | 5 | 0 | 0 | 45 | 30 | 80 | 0 | 4 |
| 53 | 1.491 | 0 | 0 | 25 | 25 | 32 | 82 | 0 | 3 |
| 52 | 0.656 | 10 | 4 | 50 | 8 | 16 | 88 | 0 | 3 |
| 51 | 0.531 | 27 | 63 | 0 | 1 | 2 | 93 | 0 | 2 |
| | | | | occupied | | | | | |
| 50 | 0.000 | 49 | 25 | 10 | 6 | 0 | 90 | 0 | 2 |

**Table 7.** Comparison of the Calculated Ground State Parameters to the Experimental Values for Reduced $\Delta^9$D

| | exp | | calcd | |
|---|---|---|---|---|
| | FeB | FeA | FeB | FeA |
| $J$ ($cm^{-1}$) | −1.0 | | −4.5 | |
| $D$ ($cm^{-1}$) | $-10 \pm 5$ | $-10 \pm 5$ | −2.4 | −3.5 |
| $\lvert E/D \rvert$ | | | 0.02 | 0.03 |

**Table 8.** Comparison of the Calculated Ligand Field Transition Energies to the Experimental Values for Reduced $\Delta^9$D

| | exp | | LF calcd | | ADF calcd | |
|---|---|---|---|---|---|---|
| level | FeB | FeA | FeB | FeA | FeB | FeA |
| $x^2-y^2$ | 10080 | 10080 | 10000 | 10100 | 11000 | 11000 |
| $z^2$ | 7030 | 7030 | 6900 | 6900 | 6900 | 6100 |
| *xy* | | | 4700 | 4900 | 3400 | 3500 |
| *xz* | | | 1400 | 1200 | 1100 | 1300 |
| *yz* | | | 0 | 0 | 0 | 0 |

These calculations were evaluated by comparison to the following experimental data: (1) The ground-state exchange coupling constant $J$ was estimated[82] to be $J = -4.5$ $cm^{-1}$ from the difference of the $E_{tot}$ between the HS and BS states, indicating that the two iron sites are weakly antiferromagnetically coupled. This is in agreement with experiment (Table 7), and is again consistent with the low composition of the bridging carboxylate ligand orbitals in the d-based levels (Table 6). (2) The energies of the spin-allowed ligand field transitions of each Fe were calculated and compared to those obtained from the CD/MCD studies and ligand field calculations (Table 8).[39] The results are consistent among the three approaches, suggesting that the bond lengths of the geometry-optimized structure are close to those of the protein active site structure. (3) The $D$ tensor matrix elements were estimated[83] from the calculated MO compositions and the energies of the ligand field transitions. The principal axes of the tensors are shown in Figure 8B, and Table 7 compares the calculated ZFS parameters to those obtained from VTVH MCD and spin-Hamiltonian analysis.[39] The negative signs of the two $D$s are consistent with experiment and the fact that the two iron centers have square-pyramidal geometries. Their magnitudes, however, are smaller than the experimental values. This result indicates that the energy splitting of the $^5T_{2g}$ state is too high (vide supra), which would decrease spin−orbit coupling interactions within the ground state.

The results presented above for reduced $\Delta^9$D are consistent with the crystal structure.[16] They indicate that the two iron centers are approximately equivalent with 5C distorted square-pyramidal geometries with both *z*-axes along the Fe−$N_{His}$ bonds. The extra electrons are in the *yz*-based ground states of both irons, and the first excited states are again at low energy (at ∼1100 and 1300 $cm^{-1}$). Figure 10B gives the redox-active orbitals of reduced $\Delta^9$D. Relative to those of reduced RR, the orbitals on FeB are similar while that on FeA for reduced $\Delta^9$D is rotated such that none of the lobes is along the *z* direction. This could affect the orbital overlap when the active site interacts with dioxygen (vide infra). Comparison of the $E_{tot}$ of reduced RR and reduced $\Delta^9$D (from the BS calculations) reveals that reduced RR is at higher energy than reduced $\Delta^9$D (by 1.21 eV). The major difference between the two reduced structures **(**Figure 8) is that one of the iron centers in reduced RR is 4C in the energy-minimized structure. This suggests that the protein environment may constrain bidentate coordination of carboxylate at this iron center.[84] The lower coordination number of this iron leads to less energy stabilization as less charge is donated to the metal center. The structural and energy differences between reduced RR and reduced $\Delta^9$D are summarized at the left in Scheme 1.

**C. Dioxygen Reactivity.** Kinetic and spectroscopic studies have shown that reactions of the reduced form of site-directed mutated RR and chemically reduced $\Delta^9$D in the presence of substrate with dioxygen result in formation of $\mu$-1,2 peroxo-bridged binuclear ferric intermediates.[21,25,26] In addition, kinetic evidence has also indicated the presence of a similar peroxo intermediate in reduced RR.[85] This requires two-electron transfer from the binuclear ferrous center to the two half-occupied antibonding $\pi^*$ orbitals of dioxygen. This electron-transfer process can be achieved by a number of possible pathways including the following: (1) reaction of dioxygen at one of the irons with transfer of one electron to form a superoxide or transfer of two electrons to form peroxide where the second electron derives from the noncoordinated iron through the carboxylate superexchange pathway and (2) direct reaction of dioxygen with both irons in a bridging mode with two-electron transfer to form a $\mu$-peroxo complex. Note that the second pathway requires a reorientation of the two $\mu$-1,3 carboxylate bridges relative to that in the reduced form to form a peroxo-bridged structure similar to that of the structurally defined peroxo model complexes (vide infra). Thus, to evaluate these two possible intermediates (superoxide- and peroxo-bound complexes), broken symmetry calculations were performed on the active site of RR at three stages: (1) dioxygen was bound to one iron center in an end-on fashion (Scheme 1, top), (2) the dioxygen was bound to both irons in a $\mu$-1,2 bridging configuration without altering the orientation of the carboxylate bridges in the reduced structure (Scheme 1, center), and (3) the dioxygen was bound to both irons in a $\mu$-1,2 bridging configuration with a rearrangement of the carboxylate bridges to a structure consistent with those of peroxo-bridged model complexes (Scheme 1, right). Parallel calculations were performed on the active site of $\Delta^9$D with $O_2$ bound in a $\mu$-1,2 bridging mode

(84) Moving the unbound oxygen of this carboxylate to be within 2.4 Å of the Fe results in a 5-coordinate site with a lower $E_{tot}$ of −157.82 eV.

(85) Tong, W. H.; Chen, S.; Lloyd, S. G.; Edmondson, D. E.; Huynh, B. H.; Stubbe, J. *J. Am. Chem. Soc.* **1996**, *118*, 2107−2108.

**Scheme 1**

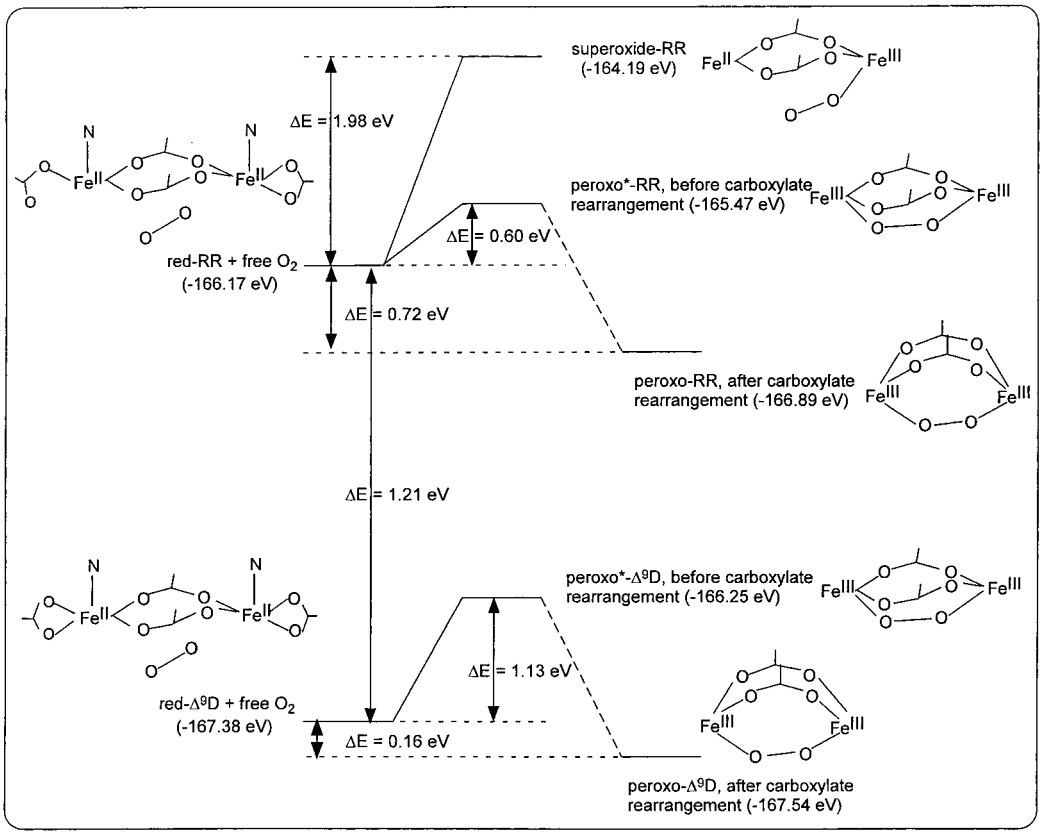


**Table 9.** Summary of the Voronoi Charges from the BS Calculations ($M_s = 0$) for RR and $\Delta^9$D

| | FeB (5C) | FeA (4C) | O1 | O2 | $Glu_{bridge}$ | $Glu_{terminal}$ |
|---|---|---|---|---|---|---|
| reduced RR | 1.34 | 1.35 | 0 | 0 | −1.36 | −1.38 |
| $O_2$-RR | 1.46 | 1.39 | −0.26 | −0.17 | −1.24 | −1.27 |
| peroxo*-RR | 1.48 | 1.46 | −0.40 | −0.36 | −1.09 | −1.09 |
| peroxo-RR | 1.55 | 1.50 | −0.46 | −0.38 | −1.06 | −1.16 |
| | FeB (5C) | FeA (5C) | O1 | O2 | $Glu_{bridge}$ | $Glu_{terminal}$ |
| reduced $\Delta^9$D | 1.32 | 1.30 | 0 | 0 | −1.40 | −1.37 |
| peroxo*-$\Delta^9$D | 1.44 | 1.42 | −0.25 | −0.26 | −1.22 | −1.20 |
| peroxo-$\Delta^9$D | 1.63 | 1.55 | −0.44 | −0.40 | −1.17 | −1.17 |

without and with alteration of the carboxylate bridges to investigate the origin of the difference in dioxygen reactivity between RR and $\Delta^9$D (Scheme 1, center and right). Each structure was geometry optimized to obtain a minimum $E_{tot}$ (final coordinate are given in the Supporting Information).

**(a) $O_2$ Reaction at One Iron Center.** Figure 12A shows the geometry-optimized one iron-bound oxy-active site of RR ($O_2$-RR). Dioxygen is found to selectively bind to the 5C site (FeB) in the energy-minimized structure, consistent with the fact that the 5C site is coordinatively unsaturated but has one more ligand thus can donate more negative charge to $O_2$. The structure obtained has Fe−O and O−O bond lengths of 1.80 and 1.32 Å, respectively, indicating that $O_2$ is bound as superoxide. Table 9 compares the differences in the Voronoi charge[86] between reduced RR and $O_2$-RR. The relative values

(86) Voronoi charge analysis consists of assigning the charge density at a given point in space to the nearest atom. Thus it is inappropriate to compare absolute numbers. Changes in charge density, however, do give reasonable insight into the effect of bonding on the location of charge densities. Reference 54.

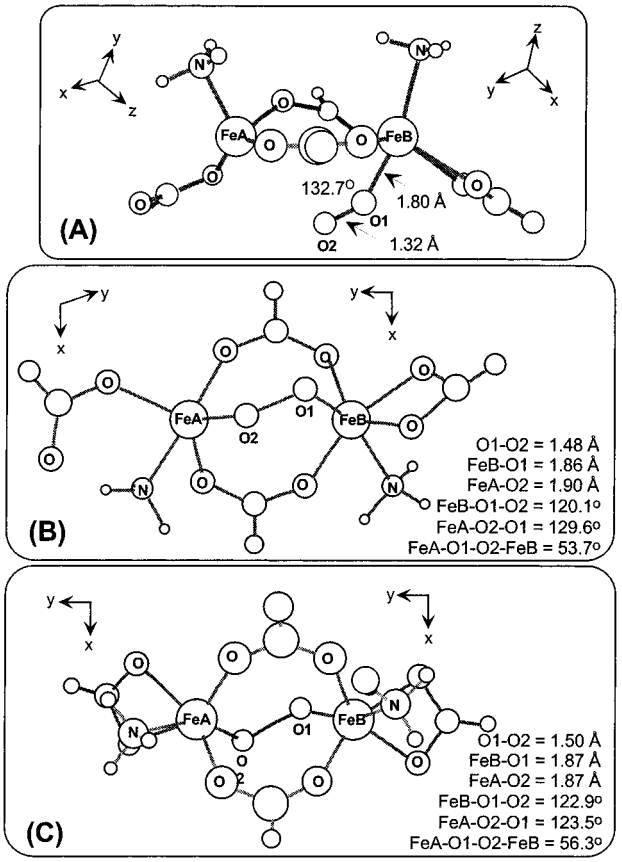


**Figure 12.** Energy minimized binuclear active site structures of (A) $O_2$-RR, (B) peroxo-RR, and (C) peroxo-$\Delta^9$D. The axes indicated are the principal directions of the *D* tensors. Key structural features are indicated or listed in the insets.

**Table 10.** Energy (eV) and Composition (%) of the Relevant Fe d-based MOs Obtained from a BS Calculation on Oxygen Bound to One Iron in RR

| Spin-Up, Localized at FeB | | | | | | | | |
|---|---|---|---|---|---|---|---|---|
| | | | | superoxide | | | | |
| level | energy (eV) | FeB | FeA | O1 | O2 | orbital | $Glu_{bri}$ | $Glu_{ter}$ |
| unoccupied | | | | | | | | |
| $x^2 - y^2$ | −2.481 | 66 | 0 | 4 | 11 | | 6 | 12 |
| $z^2$ | −3.493 | 63 | 0 | 5 | 6 | $\pi^*_\nu$ | 7 | 15 |
| $xy$ | −3.555 | 63 | 0 | 17 | 16 | $\pi^*_\nu$ | 1 | 2 |
| $xz$ | −3.755 | 59 | 3 | 13 | 12 | $\pi^*_\nu$ | 4 | 7 |
| $yz$ | −4.268 | 69 | 0 | 11 | 8 | $\pi^*_\nu$ | 3 | 8 |
| total % of $\pi^*_\nu$: 88% | | | | | | | | |

| Spin-Down, Localized at FeA | | | | | | | | |
|---|---|---|---|---|---|---|---|---|
| | | | | superoxide | | | | |
| level | energy (eV) | FeB | FeA | O1 | O2 | orbital | $Glu_{bri}$ | $Glu_{ter}$ |
| unoccupied | | | | | | | | |
| $xz$ | −2.410 | 0 | 80 | 0 | 0 | | 4 | 15 |
| $yz$ | −2.949 | 0 | 71 | 0 | 0 | | 7 | 20 |
| $xy$ | −3.480 | 1 | 72 | 0 | 1 | | 7 | 16 |
| $z^2$ | −3.678 | 0 | 88 | 0 | 0 | | 4 | 5 |
| | −4.072 | 27 ($z^2$) | 7 ($x^2 - y^2$) | 26 | 27 | $\pi^*_\sigma$ | 4 | 7 |
| occupied | | | | | | | | |
| $x^2 - y^2$ | −4.253 | 2 | 87 | 3 | 1 | | 4 | 3 |
| total % of $\pi^*_\sigma$: 53% | | | | | | | | |

indicate that charge is transferred from FeB (5C) (and the bridging and terminal glutamate residues) to oxygen while the charge on FeA in both species is approximately the same. The amount of charge transferred to $O_2$ is about half of that for the bridged peroxo species (peroxo-RR in Table 9, vide infra). This is consistent with the formation of a superoxide bound to a ferric ion in $O_2$-RR.

Table 10 presents the energy and composition of the relevant Fe d-based MOs obtained from a BS calculation on the energy-minimized $O_2$-RR structure. Reaction of dioxygen with one iron results in significant electron redistribution to the dioxygen. It should be noted that exchange stabilization of the Fe d-based occupied MOs results in significant mixing with ligand-based orbitals, which complicates a direct analysis of the occupied orbitals. The metal−ligand bonding interacting can, however, be inferred from the Fe d-based unoccupied MOs that are metal−ligand antibonding in nature. Also note that a large contribution from terminal glutamate residues was found in the occupied Fe d-based MOs (Table 10), which is likely due to an overestimate of covalency by the DFT calculations.[87−93] Thus the nature of the superoxide complex should be reflected in the composition of the two oxygen atoms in the unoccupied d-based MOs shown in Table 10. Coordination of dioxygen to the FeB center results in a split in energy of the highest occupied $\pi^*$ orbitals of $O_2$ into two nondegenerate levels, designed $\pi^*_\nu$ and $\pi^*_\sigma$ with the $\pi^*_\sigma$ being the most stabilized in energy due to its stronger $\sigma$ bonding interaction with FeB. In Table 10, it is found that the total composition of the spin-up $\pi^*_\nu$ orbital is approximately 90% while that of the spin-down $\pi^*_\sigma$ orbital is about 50%. This indicates that most of the charge is transferred from a spin-down FeB orbital to the spin-down $\pi^*_\sigma$ orbital. This $\pi^*_\sigma$ orbital has good $\sigma$ overlap with the formally spin-down, occupied $z^2$ orbital of FeB that is at high energy (note that $O_2$ binds to FeB along the $z$-axis that is also approximately along the Fe−$N_{His}$ bond). Thus electron density is transferred from this $z^2$ orbital to the $\pi^*_\sigma$ orbital of dioxygen, and the net effect is to produce an $Fe^{III}$ with a $(t_2)^4(e)^1$ configuration that is an excited quartet state. This requires a significant amount of excitation energy that is reflected in the $E_{tot}$ of the superoxide complex (−164.49 eV). Figure 13 shows the surface plot of the spin-down LUMO that has 53% composition from the $\pi^*_\sigma$ orbital of dioxygen. It should be noted that this orbital has only a small contribution from the unbound FeA and a low composition of the bridging carboxylate ligands reflecting a poor superexchange pathway. Thus a second electron is not transferred from $Fe^{II}$ (FeA).

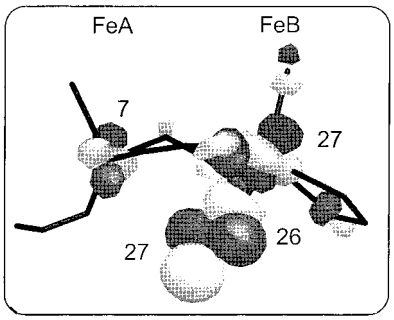


**Figure 13.** Surface plots of the lowest unoccupied spin-down MOs of $O_2$-RR obtained from a BS ($M_s = 0$) calculation. The O p and Fe d orbital contributions are indicated.

The results presented above show that terminal binding of dioxygen to FeB (5C) of reduced RR results in a superoxide−$Fe^{III}$ complex. This one-electron transfer results in an excited state on the $Fe^{III}$ and thus a significantly higher $E_{tot}$ (−164.19 eV) compared to the sum of the $E_{tot}$ for reduced RR and free dioxygen (−166.17 eV), Scheme 1, top. The second electron transfer that would help stabilize this possible intermediate is not observed due to the poor superexchange pathway associated with carboxylate bridges.

**(b) Bridged $O_2$.** In this section we allow dioxygen to react with reduced RR and $\Delta^9$D in a $\mu$-1,2 bridging mode. Broken symmetry calculations were performed on geometry-optimized $O_2$-bridged RR and $\Delta^9$D structures before and after the rearrangement of the position of the carboxylate bridges (Scheme 1, center and right). The distances between the iron atoms and the orientations of the dioxygen relative to the binuclear active site were allowed to vary within a reasonable range of those present in a series of structurally defined peroxo-model complexes (final coordinates are given in the Supporting Information).[94]

Binding of dioxygen in a $\mu$-1,2 bridging mode without the rearrangement of the two $\mu$-1,3 carboxylate bridges relative to that in the corresponding reduced forms generates species with a short O−O bond length (1.40 Å for RR and 1.32 Å for $\Delta^9$D) at a higher energy than the reduced site plus free $O_2$ (0.60 eV for RR and 1.31 eV for $\Delta^9$D, Scheme 1, center). In addition, the charge distribution for these two species is different from that of their corresponding peroxo forms after the carboxylate rearrangement (vide infra). Table 9 compares the Voronoi charge of these $O_2$-bridged species to those after carboxylate rearrangement (peroxo* vs peroxo). The amount of charge transferred to $O_2$ from both irons is about equal, and the charge

(87) Henson, M. J.; Mukherjee, P.; Stack, T. D. P.; Solomon, E. I. *J. Am. Chem. Soc.* **1999**, *121*, 10332−10345.
(88) Hanson, M. H.; Solomon, E. I. Unpublished results.
(89) Becke, A. D. *J. Chem. Phys.* **1993**, *98*, 5612.
(90) Ziegler, *Chem. Rev.* **1991**, *91*, 651.
(91) Ziegler, *Can. J. Chem.* **1995**, *73*, 743.
(92) Siegbahn *Adv. Chem. Phys.* **1996**, *93*, 333.
(93) Li, J.; Noodleman, L.; Case, D. A. *Inorganic Electronic Structure and Spectroscopy*; Solomon, E. I., Lever, A. B. P., Eds.; Wiley-Interscience: New York, 1999, pp 661−724.
(94) Brunold, T. C.; Tamura, N.; Kitajima, N.; Morooka, Y.; Solomon, E. I. *J. Am. Chem. Soc.* **1998**, *120*, 8724−8738.

**Table 11.** Energy (eV) and Composition (%) of the Relevant Fe d-based MOs Obtained from a BS Calculation on Peroxo-Bound RR

| Spin-Up, Localized at FeB (5C) | | | | | |
|---|---|---|---|---|---|
| | | | peroxide | | |
| level | energy (eV) | FeB | O1 | O2 | orbital |
| | | unoccupied | | | |
| $z^2$ | −3.409 | 68 | 5 | 1 | |
| $xz$ | −4.202 | 66 | 16 | 5 | $\pi^*_\sigma$ |
| $yz$ | −4.446 | 74 | 13 | 3 | $\pi^*_\nu$ |
| $x^2 - y^2$ | −4.890 | 82 | 1 | 4 | |
| $xy$ | −5.027 | 79 | 6 | 2 | |
| Spin-Down, Localized at FeA (4C) | | | | | |
| | | | peroxide | | |
| level | energy (eV) | FeA | O1 | O2 | orbital |
| | | unoccupied | | | |
| $z^2$ | −3.857 | 67 | 3 | 15 | $\pi^*_\sigma$ |
| $yz$ | −4.376 | 74 | 1 | 1 | |
| $x^2 - y^2$ | −4.633 | 67 | 5 | 16 | $\pi^*_\nu$ |
| $xz$ | −4.818 | 74 | 5 | 8 | |
| $xy$ | −5.128 | 91 | 0 | 0 | |

donation is less than that for the bridged peroxo species after the rearrangement. Also note that the amount of charge transferred for RR is more than that for $\Delta^9$D, consistent with the longer O−O bond length obtained for RR. The above results suggest that the orientation of the carboxylate bridges in the reduced structures provides a steric constrain. The carboxylate rearrangement is required to obtain peroxo-RR and peroxo-$\Delta^9$D with structures similar to those of the peroxo model complexes. This lowers the energy below that of the reduced site plus $O_2$ (vide infra). Thus binding of dioxygen in a bridging mode without carboxylate rearrangement gives a larger activation barrier for the formation of $O_2$-bridged $\Delta^9$D from reduced $\Delta^9$D plus dioxygen than that for RR (Scheme 1, center), which is consistent with the very low kinetic reactivity of this reduced site.

With the carboxylate rearranged to an orientation similar to that for the peroxo model complexes, a similar optimized $O_2$-bridged active site structure was obtained for RR and $\Delta^9$D (Figure 12B,C). The Fe−O and O−O bond lengths (1.87 and 1.49 Å average) and Fe−O−O angle (120−130°) are reasonable and indicate that binding of dioxygen to reduced RR and $\Delta^9$D in a $\mu$-1,2 bridging configuration with the carboxylate rearrangement results in peroxo complexes. Table 9 compares the Voronoi charge between the reduced and the $O_2$-bridged forms of peroxo-RR and peroxo-$\Delta^9$D. It shows that in both RR and $\Delta^9$D similar charge is transferred from both irons to dioxygen, consistent with the formation of peroxo-bridged complexes. Furthermore, both peroxo-RR and peroxo-$\Delta^9$D are stabilized from their corresponding reduced site (−0.72 eV for RR and −0.16 eV for $\Delta^9$D, Scheme 1, right) with peroxo-RR at lower energy.

Different charge donation is observed for $O_2$-bridged RR and $\Delta^9$D both before (results are given in the Supporting Information) and after (Table 11) the carboxylate rearrangement. Table 11 summarizes the energy and composition of the relevant Fe d-based MOs obtained from a BS calculation on peroxo-RR. Five unoccupied d-based MOs are observed in both the spin-up and spin-down manifolds, indicating that the binuclear center has transferred two electrons to dioxygen, resulting in a binuclear ferric−peroxo complex. The results show that the compositions of the oxygen atoms in the redox active MOs (ground low lying first excited state) of both spins are approximately the same (37% in spin up and 39% in spin down). The total compositions

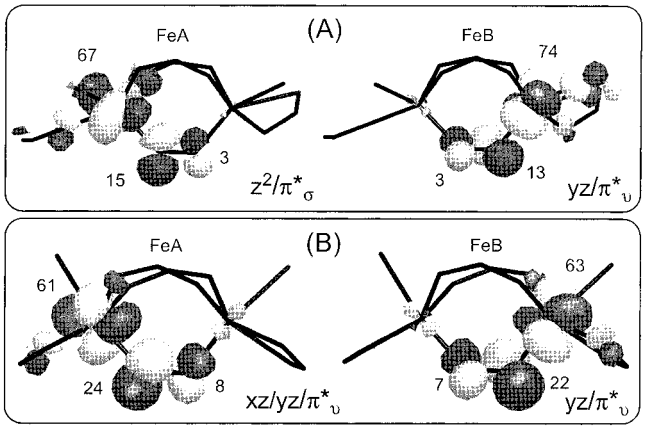


**Figure 14.** Surface plots of the unoccupied Fe d-based MOs relevant to the peroxide $\pi^*$-based occupied MOs from a BS ($M_s = 0$) calculation on (A) peroxo-RR and (B) peroxo-$\Delta^9$D. The O p and Fe d orbital contributions are indicated.

**Table 12.** Energy (eV) and Composition (%) of the Relevant Fe d-Based MOs Obtained from a BS Calculation on Peroxo-Bound $\Delta^9$D

| Spin-Up, Localized at FeB | | | | | |
|---|---|---|---|---|---|
| | | | peroxide | | |
| level | energy (eV) | FeB | O1 | O2 | orbital |
| | | unoccupied | | | |
| $z^2$ | −3.046 | 67 | 11 | 4 | |
| $x^2 - y^2$ | −3.639 | 74 | 2 | 0 | |
| $yz$ | −4.173 | 63 | 22 | 7 | $\pi^*_\nu$ |
| $xy$ | −4.650 | 86 | 3 | 3 | |
| $xz$ | −4.755 | 86 | 2 | 2 | |
| Spin-Down, Localized at FeA | | | | | |
| | | | peroxide | | |
| level | energy (eV) | FeA | O1 | O2 | orbital |
| | | unoccupied | | | |
| $z^2$ | −3.143 | 69 | 2 | 12 | |
| $x^2 - y^2$ | −3.740 | 75 | 0 | 1 | |
| $xz/yz$ | −4.191 | 61 | 8 | 24 | $\pi^*_\nu$ |
| $xy$ | −4.573 | 87 | 4 | 1 | |
| $yz/xz$ | −4.657 | 85 | 1 | 2 | |

of the $\pi^*_\sigma$ and $\pi^*_\nu$ orbitals from both spins are also very similar (39% for $\pi^*_\sigma$ and 37% for $\pi^*_\nu$), indicating that the two irons transfer approximately the same amount of charge to these two orbitals. The charge is transferred from the ground states ($yz/xz$ for FeB and $z^2/yz$ for FeA), or a low-lying excited level ($xz/yz$ for FeB and $x^2 - y^2$ for FeA) of the reduced site. Thus two electrons are transferred into the $\pi^*_\nu$ and $\pi^*_\sigma$ orbitals of dioxygen, respectively. Figure 14A shows the contour plots of the spin-up, unoccupied $yz$-based MO from FeB and the spin-down, unoccupied $z^2$-based MO from FeA.

A very different behavior, however, is observed in peroxo-$\Delta^9$D. Table 12 shows the energy and composition of the relevant Fe d-based MOs from a BS calculation on peroxo-$\Delta^9$D. The binuclear center again transfers two electrons to dioxygen and a similar binuclear ferric−peroxo active site is obtained. The compositions of the oxygen atoms in the redox active MOs (ground-state yz and low-lying excited-state xz/yz) from both spins are also found to be similar (29% in spin up and 32% in spin down). However, the binuclear center transfers both of these electrons (one from the $yz$-based ground state of FeB and another from a low-lying $xz/yz$-based excited state of FeA) into the spin-up and spin-down $\pi^*_\nu$ orbitals of the dioxygen. Figure 14B shows the contour plots of the $yz$-based, spin-up unoccupied

MO from FeB and the *xz*/*yz*-based, spin-down unoccupied MO from FeA. Transferring both electrons into the $\pi^*_\nu$ orbital of dioxygen requires that both of the electrons in the $O_2$ molecule be spin-paired in the $\pi^*_\sigma$ orbital. This results in less stabilization of peroxo-$\Delta^9$D ($-0.16$ eV) relative to peroxo-RR ($-0.72$ eV) referenced to their corresponding reduced sites, Scheme 1, right. Thus reaction of RR with dioxygen to form the peroxo-bound species is favored by $-0.56$ eV relative to the reaction of reduced $\Delta^9$D with $O_2$. Combined with the fact that binding of dioxygen results in a higher activation barrier for $\Delta^9$D (vide supra), the results are consistent with a higher dioxygen reactivity for RR.

In summary, binding of dioxygen to reduced RR in an end-on fashion results in a significantly higher energy than with a $\mu$-1,2 bridging configuration, indicating that the formation of a bridged $O_2$-bound intermediate is energetically favorable. A rearrangement of the $\mu$-1,3 carboxylate bridges is further required for the formation of peroxo-RR and peroxo-$\Delta^9$D. Importantly, compared to $\Delta^9$D, the formation of peroxo-RR has a lower kinetic barrier and is energetically more favorable. This appears to result from the fact that the difference in the ligand field of one of the irons in the reduced sites between RR and $\Delta^9$D changes its redox-active orbital (Section 2B) which affects the ability of the active site to transfer the second electron to dioxygen bound in a $\mu$-1,2 bridging mode.

## Discussion

The $Fe^{II}$ binding titration and MnFe mixed-metal derivative studies have defined the spectral features of each iron center in reduced RR. The two sites have different iron binding affinities. The site with higher affinity exhibits one ligand field transition at $\sim$9500 $cm^{-1}$ and has a negative ZFS indicating that it must be 5C consistent with its higher affinity. The site with lower affinity has two ligand field transitions at about 5500 and 7000 $cm^{-1}$ and a positive ZFS, consistent with a 4-coordinate site. Several observations suggest that the 5C (FeB) center is the site containing the Glu204 residue (on Fe2, Figure 1B). Correlation of the relative affinities of the $Fe^{II}$ sites, the different Mössbauer parameters of the oxidized sites, and the crystallographically determined geometries of the oxidized sites were previously cited in favor of this correlation.[51] Additional support is provided by (1) spectroscopic studies on a site-directed mutant of R2 in which D84 (an Fe1 ligand, Figure 1B) is replaced with glutamate (E), where the two low-energy transitions are perturbed but the 9500 $cm^{-1}$ remains unchanged,[95] and (2) the observation of disorder of Glu204 in the crystal structure of reduced RR, which make this a candidate for additional bidentate coordination to Fe2 (relative to the crystal structure).[15] Thus the active site of reduced RR under spectroscopic conditions of pH 7.6 and 0.15 M Hepes buffer can be best described as containing one 5C and one 4C iron with the 5C site having a bidentate Glu204 ligand. Chemical perturbation studies, however, show that the site can be perturbed by a change in pH or the addition of NaCl. In the presence of low pH (5−6) and high salt (conditions of the crystal structure), the terminal glutamate could undergo protonation and thus shift to monodentate coordination to Fe2 (Figure 1B). To further correlate the spectroscopy to the crystallography, it would be extremely useful to (1) obtain spectroscopic data on the crystals and (2) obtain a crystal structure under conditions more nearly approximating those used in the spectroscopic and reactivity studies.

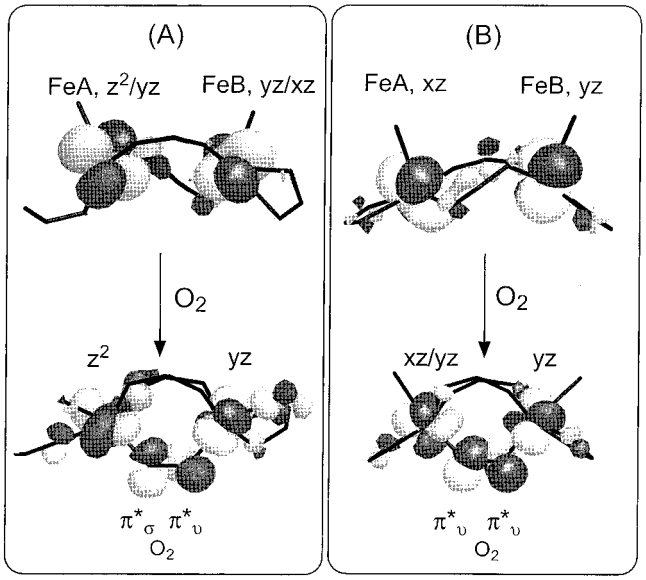


**Figure 15.** Formation of peroxo-bound complexes by charge donation from the orbitals of the reduced sites into the $\pi^*$ orbitals of dioxygen (A) RR and (B) $\Delta^9$D. Top: The occupied MOs of the reduced active sites. Bottom: The unoccupied MOs of the peroxo-bound complexes.

Spectroscopy and crystallography combined with density functional calculations provide geometric and electronic structure insight into reduced RR and reduced $\Delta^9$D. Their difference in reactivity can in part be related to the difference in their redox active orbitals. The Fe2 sites of the two reduced forms are both 5-coordinate with a distorted square-pyramidal geometry (Figure 1B and C), giving a *yz*-based doubly occupied ground orbital with similar orientations (Figure 10, right side orbitals). The presence of a 4C site in reduced RR, however, changes the ligand field at that Fe, which results in a different doubly occupied orbital orientation relative to that of the second 5C site in reduced $\Delta^9$D (Figure 10, left side orbitals). The doubly occupied orbital for the 4C site in reduced RR is rotated such that one of the lobes is along the FeA$-O_2$ bond (Figure 12B), resulting in a better orientation for the $\sigma$ interaction between FeA and $O_2$ (Figure 15A, bottom). These calculations also indicate that the energy of reduced RR is higher than that of reduced $\Delta^9$D. This difference relates to the lower coordination environment of one Fe (FeA, 4C) in reduced RR that could arise from a constrained protein environment. The presence of a 4C center in reduced RR destabilizes the active site and could contribute to its high dioxygen reactivity.

From these calculations, binding dioxygen in an end-on configuration to one iron in reduced RR would result in one-electron transfer from the reduced site to form a superoxide complex. Due to $\sigma$ orbital overlap, the electron is transferred from the $z^2$ orbital ($z = N_{His}-Fe-O_2$ axis), resulting in a quartet $Fe^{III}$ excited state and thus a high-energy barrier. Furthermore, transfer of a second electron from the iron not directly coordinated to $O_2$ is not observed, indicating that the $\pi/\sigma$ superexchange pathways associated with the carboxylate bridges are poor in contrast to what is observed for hemerythrin where the bent oxo-bridge allows a second electron transfer (Figure 16) and that the formation of peroxide is stabilized by bridged binding.[96] These calculations suggest that the formation of superoxide is energetically uphill by $\sim$2 eV and that the formation of a $\mu$-1,2-bridged peroxo intermediate is energetically more favorable.

(95) Yang, Y.-S.; Baldwin, J.; Ley, B. A.; Bollinger, J. M., Jr.; Solomon, E. I. Manuscript in preparation.

(96) Brunold, T. C.; Solomon, E. I. *J. Am. Chem. Soc.* **1999**, *121*, 8277−8287.

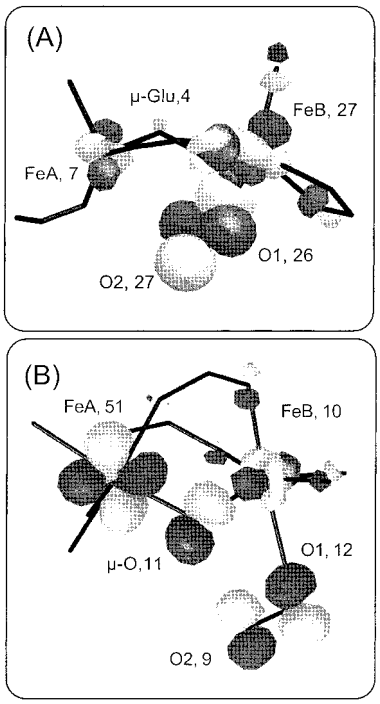


**Figure 16.** Comparison of the $\pi/\sigma$ superexchange pathways for (A) $O_2$-RR and (B) $O_2$-Hr. The O p and Fe d orbital contributions are indicated. Note that the FeB−O1 distance is 1.80 Å in $O_2$-RR, while the FeB−O1 distance is 2.95 Å in $O_2$-Hr. Part B is reprinted from JACS (1999, ref 96).

Binding of dioxygen in a bridged mode without the rearrangement of the carboxylate bridge results in an energy barrier that is lower for RR than $\Delta^9$D. The carboxylate bridges likely cause a steric hindrance, which prevents complete two-electron transfer from the two irons to dioxygen. Reaction of dioxygen in a bridged geometry with the carboxylate rearrangement forms a peroxo-bound species. Different two-electron charge donations to dioxygen are observed for peroxo-RR and peroxo-$\Delta^9$D. In peroxo-RR, the two electrons are transferred from the ground and low-lying excited states to the $\pi^*_\nu$ and $\pi^*_\sigma$ orbitals of dioxygen. In contrast, in peroxo-$\Delta^9$D both electrons from the ground and low-lying excited states of the iron sites are transferred only into the peroxy $\pi^*_\nu$ orbital. This derives from the different orientations of the redox active orbitals of the two irons of the reduced sites (Figure 15). In both sites one iron has the same *yz*-based redox orbital while the redox orbitals for the other iron are different due to the different ligand fields in the 4C vs the 5C structures (vide supra). Transferring two electrons from reduced $\Delta^9$D into the $\pi^*_\nu$ orbital of dioxygen requires spin pairing of the two electrons in the $\pi^*_\sigma$ orbital of dioxygen, resulting in less stabilization of peroxo-$\Delta^9$D compared to peroxo-RR. Thus compared to $\Delta^9$D, binding of dioxygen to reduced RR in a $\mu$-1,2 configuration provides a lower kinetic barrier and a thermodynamically more stabilized product. This is consistent with the higher intrinsic reactivity of the reduced site of RR relative to $\Delta^9$D observed experimentally.

It should be noted that since geometry optimization of the $O_2$-bridged species does not directly lead to the rearrangement of the carboxylate bridges, it is likely that there is an additional Franck−Condon barrier associated with this carboxylate rearrangement (between the center and right in Scheme 1) that should be very similar for both RR and $\Delta^9$D but could be influenced by differences in protein environment. In addition, the reaction coordinates utilized in these calculations consistently have one ligand less in RR than in $\Delta^9$D. Binding of dioxygen to reduced $\Delta^9$D in a bridging mode results in coordination saturation for both iron sites (6C+6C), while $O_2$-bridged RR has one open coordination site (5C+6C) that allows the possibility of the monodentate terminal carboxylate to bind bidentate when the site is oxidized by $O_2$, which can further stabilize the product and contribute to the increased reactivity of RR.

The low dioxygen reactivity of reduced $\Delta^9$D, however, has been found to be greatly enhanced by substrate binding.[26,38] CD and MCD studies showed that substrate binding strongly perturbs the active site structure.[39] In the presence of substrate, new transitions are observed at 5500 and 8500 $cm^{-1}$, indicating that one of the irons has changed to 4-coordinate, and is very similar to that observed for reduced RR. Spectral features very similar to those of substrate-bound $\Delta^9$D have now also been observed for the D84E mutant of RR[95] and reduced RR from mouse.[97] Thus, it appears that there is a similar active site structure for the reduced binuclear sites with high dioxygen reactivity in RR and $\Delta^9$D. While the crystal structures of the resting reduced sites of $\Delta^9$D and RR are different, under conditions where the sites are reactive with dioxygen these sites appear to become similar, consistent with the formation of similar peroxo intermediates. The reactive structure appears to have one 5C and one 4C iron center bridged with two $\mu$-1,3 carboxylates with the redox active orbitals of both irons having good overlap with the two-half-occupied $\pi^*$ orbitals of dioxygen bound in a $\mu$-1,2-bridging mode.

In the present study the binuclear active site geometric and electronic structures of reduced RR and reduced $\Delta^9$D have been investigated and electronic contributions to differences in their dioxygen reactivity have been explored. It is now of importance to correlate these results to the other dioxygen activating enzyme, methane monooxygenase (MMO), to gain insight into structure/function correlations among the three enzymes presently known to be in this class.

**Acknowledgment.** We thank Prof. Thomas Brunold for useful discussions. Financial support by the NSF-Biophysics Program Grant MCB 9816051 (E.I.S.) and NIH GM-55365, the Searle Scholar's Program of the Chicago Community Trust, and the Camille and Henry Dreyfus Foundation (J.M.B.).

**Supporting Information Available:** Cartesian coordinates of the models used for the calculations, energy and MO compositions for $O_2$-bridged RR and $\Delta^9$D before the carboxylate rearrangement, VTVH MCD simulation of MnFe-RR, and MCD spectrum of MnFe-RR (PDF). This material is available free of charge via the Internet at http://pubs.acs.org.

JA994406R

(97) Strand, K. R.; Yang, Y.-S.; Andersson, K. K.; Solomon, E. I. Unpublished results.